National Defence / Défense nationale

(1)

ANALYSIS OF THE NORTH TRURO SEA CLUTTER DATA (U)

by

Hing C. Chan

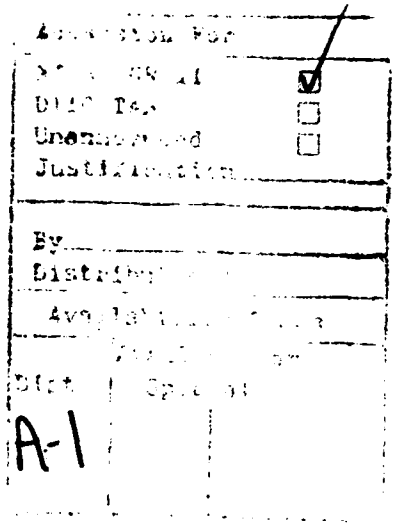

DEFENCE RESEARCH ESTABLISHMENT OTTAWA
REPORT NO.1051

Canada

December 1990
Ottawa

National Defence / Défense nationale

ANALYSIS OF THE NORTH TRURO SEA CLUTTER DATA (U)

by

Hing C. Chan
Surface Radar Section
Radar Division

DEFENCE RESEARCH ESTABLISHMENT OTTAWA
REPORT NO.1051

PCN
041LC

December 1990
Ottawa

ANALYSIS OF THE NORTH TRURO SEA CLUTTER DATA

ABSTRACT

In this report we present the results of the analysis of sea–clutter data collected at North Truro, Massachusetts by the MIT Lincoln Laboratory. The data were obtained in conditions typical of sea state 2 at X–, S–, L–bands, UHF and VHF. We examined the data both spectrally and statistically. The results showed that sea clutter exhibited very different spectral characteristics at higher frequencies compared to those at lower frequencies. Experimental sea–clutter coefficients as a function of grazing angle at various frequency bands were obtained for up–swell and cross–swell conditions. Most sea–clutter models use the radar look direction relative to the wind direction as an input parameter (e.g., up–wind, cross–wind, etc). Hence a direct comparison of sea–clutter magnitude with those calculated from models under different wind conditions was not made. Instead, we showed these results together with those calculated from two sea–clutter models, assuming up–wind and cross–wind conditions. The data were quite dissimilar in the low–grazing–angle regions to those predicted by the two models. Further research on sea clutter in the low–grazing–angle regions is needed to verify and explain the observed differences. We found the sea–clutter amplitude statistics fit the K–distribution best in the important low–probability–of–false–alarm region. The distribution approached that of a Rayleigh model for vertical polarization and low–resolution waveforms. However, there was a significant proportion of resolution cells with sea clutter having non–Rayleigh statistics even in relatively low–resolution waveforms and vertical polarization. For horizontal polarization and/or high–resolution waveforms, the statistics approached those of a lognormal model. The statistical results provided further evidence that the K–distribution can serve as a limiting distribution for sea clutter. Spatial and temporal characteristics of sea spikes were examined through the use of range–time–intensity plots of high–resolution sea clutter. The results supported the theory that sea spikes are associated with the wave crests in sea swells. This association was more evident from high–resolution, V–POL sea–clutter data. The results of this report are pertinent to shipboard radar applications where the grazing angle is low. They also provide additional information for sea–clutter modeling in the low–angle region, particularly at the lower frequency bands.

ANALYSE DES DONNÉES DU FOUILLIS DE MER DE NORTH TRURO

RÉSUMÉ

Dans ce rapport, nous présentons les résultats de l'analyse des données du fouillis de mer recueillies à North Truro au Massachusetts par le Laboratoire Lincoln du MIT. Les données ont été obtenues dans des conditions typiques à l'état de mer 2 et aux bandes de fréquences X, S, L, UHF et VHF. Nous en avons fait l'analyse spectrale et statistique. Les résultats ont montré que les caractéristiques spectrales du fouillis de mer aux hautes fréquences étaient très différentes de celles aux fréquences plus basses. Des coefficients expérimentaux pour le fouillis de mer en fonction de l'angle d'incidence rasante à différentes bandes de fréquences ont été obtenus pour une observation face aux vagues et en travers des vagues. Puisque la plupart des modèles du fouillis de mer utilisent comme paramètre d'entrée la direction d'observation du radar par rapport à celle du vent (face au vent, en travers du vent, etc), une comparaison directe de l'amplitude du fouillis de mer avec celle calculée à partir de ces modèles n'était pas possible. Nous avons plutôt comparé ces résultats avec ceux calculés à partir de deux modèles de fouillis de mer: l'un face au vent et l'autre en travers du vent. Les données correspondant à de faibles angles d'incidence rasante étaient très différentes de celles prédites par les deux modèles. Des recherches supplémentaires sur le fouillis de mer aux incidences rasantes sont nécessaires pour vérifier et expliquer les différences observées. Nous avons trouvé que la distribution statistique de l'amplitude du fouillis de mer ressemblait le plus à une distribution K dans les zones à faible probabilité de fausses alarmes soit celles de plus grande importance. Pour des formes d'onde à faible résolution et à polarisation verticale, la distribution de l'amplitude du fouillis s'approchait de la distribution de Rayleigh. Une distribution autre que Rayleigh a été aussi observée pour des formes d'onde à faible résolution et à polarisation verticale. Pour des formes d'onde à haute résolution ou à polarisation horizontale, la distribution du fouillis s'approchait d'une distribution log–normale. Les données statistiques ont fourni des preuves supplémentaires que la distribution K peut servir de cas limite pour la distribution de l'amplitude du fouillis de mer. Les caractéristiques spatio–temporelles des pointes des échos de mer ont été examinées à l'aide des diagrammes tridimentionnels de l'amplitude du fouillis de mer en fonction de la portée et du temps pour des formes d'onde à haute résolution. Les résultats soutenaient la théorie selon laquelle ces pointes sont associées aux crêtes des vagues. Cette association était encore plus évidente pour des formes d'onde à haute résolution et à polarisation verticale. Les résultats de cet article sont appropriés aux applications du radar maritime où l'angle d'incidence rasante est faible. Ils fournissent également de l'information supplémentaire sur la modélisation du fouillis de mer dans les zones où l'angle d'incidence rasante est faible, surtout aux bandes de fréquences plus basses.

EXECUTIVE SUMMARY

The performance of shipborne radars is adversely affected by returns from the sea surface surrounding the ship. These returns are called sea clutter in radar terminology. Although sophisticated signal processing techniques have been developed to minimize the interference from sea clutter, the effectiveness of these techniques is highly dependent on the characteristics of sea clutter. In order to optimize shipboard radar–signal–processing performance, a thorough understanding of the sea–clutter behaviour under a wide variety of sea conditions is required. There are two important characteristics of sea clutter which affect radar performance: (a) spectrum and (b) temporal amplitude–statistics. These characteristics change as the radar parameters and the sea conditions change.

We present in this report the results of the analysis of sea–clutter data collected at North Truro, Massachusetts by the MIT Lincoln Laboratory. The data were obtained in conditions typical of sea state 2 at X–, S–, L–bands, UHF and VHF. We examined the data both spectrally and statistically.

The results showed that sea clutter exhibited very different spectral characteristics at higher frequencies compared to those at low frequencies. At higher frequency bands (X–, S–bands), the sea clutter spectrum was generally asymmetrical with a longer spectral tail in the direction of the Doppler shift. At lower frequency bands (L–band, UHF and VHF), the sea clutter spectrum was characterized by the presence of double spectral peaks.

Experimental sea–clutter coefficients as a function of grazing angle at various frequency bands were obtained for up–swell and cross–swell conditions. Most sea–clutter models use the radar look direction relative to the wind direction as an input parameter (e.g., up–wind, cross–wind, etc). Hence a direct comparison of sea–clutter magnitude with those calculated from models under different wind conditions was not made. Instead, we contrasted these results with those calculated from two sea–clutter models, assuming an up–wind and a cross–wind conditions. The data were quite dissimilar in the low–grazing–angle regions to those predicted by the two models. Further research on sea clutter in the low–grazing–angle regions is needed to verify and explain the observed differences.

We found that the sea–clutter amplitude statistics fit the K–distribution best in the important low–probability–of–false–alarm region. The distribution approached that of a Rayleigh model for vertical polarization and low–resolution waveforms. We observed non–Rayleigh statistics even in relatively low–resolution and vertical polarization waveforms. For horizontal polarization and/or high–resolution waveforms, the statistics approached those of a lognormal model. The statistical results provided further evidence that the K–distribution can serve as a limiting distribution for sea clutter.

Spatial and temporal characteristics of sea spikes were examined through the use of range–time–intensity plots of high–resolution sea clutter. The results supported the theory that sea spikes are associated with the wave crests in sea swells. This association was more evident from high–resolution, V–POL sea–clutter data. This result also offered some clues as to the reason why the Doppler shifts of the sea clutter appeared to be greater for horizontal polarization than for vertical polarization, at least at X– and S–bands.

The results of this report are pertinent to shipboard radar applications where the grazing angle is low. They also provide additional information for sea–clutter modeling in the low–angle region, particularly at the lower frequency bands.

TABLE OF CONTENTS

LIST OF FIGURES

1. INTRODUCTION.

Sea clutter limits the performance of maritime surveillance radars. Although there exists a large body of theoretical and experimental work in the literature [1]–[4], our understanding of sea–clutter behaviour is still incomplete. A thorough understanding of sea–clutter behaviour is essential if optimum performance is to be obtained from radar signal processors. For example, the spectral characteristics will influence the design of moving target indicator (MTI) filters, and the amplitude statistics of sea clutter will influence the design of constant false alarm rate (CFAR) processors. A knowledge of the sea–clutter strength as functions of various system and environmental parameters (e.g., frequency, polarization, waveform resolution, sea state, grazing angle, etc) will enable the radar designer to tailor the signal processing to specific conditions, thereby obtaining optimal performance.

In this report we present the results of an analysis of the sea–clutter data collected by the MIT Lincoln Laboratory at North Truro, Massachusetts. This set of data was provided to Canada under a Canada–U.S. memorandum of understanding in clutter research. The results provided insights into the various mechanisms which contribute to sea–clutter returns and are particularly pertinent to shipboard radars where the grazing angle is low. Section 2 describes the radar equipment, the radar site, the resulting data base including data calibration and the signal processing techniques employed in the analysis. Section 3 describes the analysis of the sea–clutter data and discusses the results. Section 4 summarizes the findings and presents concluding remarks.

2. DATA COLLECTION AND ANALYSIS.

2.1 The Radar Equipment.

The sea–clutter data collection was carried out during a two–week period in July 1982 using the MIT Lincoln Laboratory mobile coherent radar facility[5]. The technical characteristics of this radar are summarized in Table I.

Table I : Technical Characteristics of the
MIT Lincoln Laboratory Mobile Radar Facility

Frequency (MHz)	165	430	1250	3400	9100
Azimuthal Beamwidth (Deg)	13	5	3	1	1
Range Resolution	36 m/150 m		15m / 150m		
Polarization	Vert. Transmit/Receive		Hor. Transmit/Receive		
PRF	500 Hz to 4000 Hz				
RCS Calibration Accuracy : 2 dB					

2.2 The Radar Site

The radar site was located at the North Truro Air Force Station on Cape Cod, Massachusetts. The effective radar height was 77.4 m above mean sea level. An ENDECO 949 wave–track buoy was leased and anchored 4 km off shore at 40° east of north to provide a record of the sea condition during the experiment period. The wave data were sent from a transmitter on board the buoy to a shore–based receiver for twenty minutes in each hour. These data were processed and summarized in a number of parameters such as significant wave height (SWH) and significant period (SP).

Figure 1 shows the significant wave height during the experiment period, with day "0" being July 2, 1982. The segments in the figure with no data were weekend periods when the wave buoy receiver was not in operation. The ENDECO 949 did not measure wave directions.

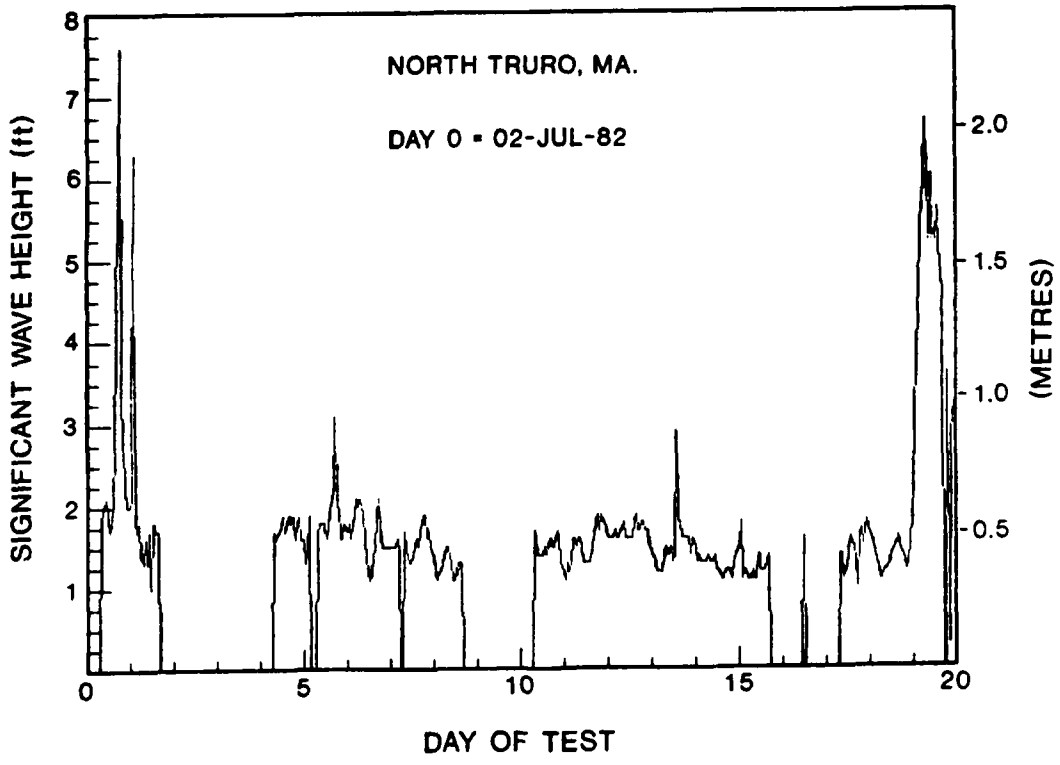

Figure 1. Variation of significant wave height during the sea–clutter experiment period.

The wind velocity readings were recorded from a location on shore at the site. The averaged wind speed was about 5 knots over the experimental period in which sea–clutter data were taken. There were isolated time intervals in which wind speeds in the 8 to 13 knots range were registered.

2.3 The Sea–Clutter Data Base

The significant wave height for most experiments ranged from 0.3 m to 0.45 m (1 to 1.5 ft). Given the limitations of the wave data and wind measurements, we could characterize the average sea condition during the experimental period only approximately, as sea state (SS) 2 (with reference to the World Meteorological Organization (WMO) code [6]). With a radar height of 77.4 m, the grazing angle for usable data was below 5 degrees. The experimental facility provided for (a) coherent data collection, (b) multi–frequency measurement, (c) near–simultaneous observation of the sea with V– and H–polarizations and (d) long–dwell–mode data collection permitting spectral and statistical measurements.

There were approximately 350 data–collection experiments, defined by the selection of frequency, polarization, waveform resolution and look direction. Data were taken in an azimuthal sector extended from 0° to 120°. All directions were measured clockwise from the north direction (0°). The analysis reported here was carried out on data of long–dwell experiments that employed a PRF of 500 Hz and dwell times of 10 to 20 seconds. Details of this data base may be found in [7].

Calibration

MIT Lincoln Laboratory personnel recorded the coherent sea–clutter data digitally and calibrated them at the Laboratory. Calibration is the process of determining the constant which relates the instantaneous analog–to–digital converter (ADC) readings to the effective radar cross–section (RCS) of the sea clutter. The calibration constant was derived from the two–way radar equation using in–situ measurement of the returns from corner reflectors of known free–space RCS values. The corner reflectors were mounted on a remote tower a few kilometers from the radar. These calibration experiments were performed for each frequency band and polarization. Since propagation of radar signals on land could be subjected to multipath effects, the calibration experiment was repeated by translating the corner reflector vertically along the length of the remote tower, thereby tracing out the interference pattern. The appropriate calibration constant was then obtained by selecting the value which yielded the best match between the theoretical and experimental interference patterns.

2.4 Signal Processing

(a) Spectral Analysis

We computed the sea–clutter spectra using the modified periodogram method [8] for X–, S– and L–bands. The long–dwell experiments for these bands employed a pulse repetition frequency (PRF) of 500 Hz and a dwell length of 10000 pulses. This provided nine 1024–point subsequences. We applied a Hamming window to each subsequence and performed the fast Fourier transform(FFT). The periodograms, which are the squared magnitudes of the FFTs, were averaged to form the sea–clutter spectrum.

For UHF and VHF, we used a specific version of the Maximum Entropy Spectral Estimation(MESE) due to Burg [9] to obtain an improved spectral resolution. The length of the time series for UHF and VHF was 5120 pulses with a 500 Hz PRF. At UHF and VHF, the spectral width of sea clutter is only a small fraction of the PRF. The spectral details of the sea clutter at these frequency could be lost due to the limited resolution of the FFT and data windowing effect.

MESE is an algorithm which provides for superior spectral resolution for random time series which can be modeled by an auto regressive (AR) system. The details of MESE are well documented [9],[10] and will not be repeated here. For the results presented in Section 3, the MESE (VHF) spectra were obtained using an AR model of order 50.

(b) Decorrelation Time

The decorrelation time of the sea clutter was obtained by measuring the time it took the envelope of the sea–clutter autocorrelation function to decay to 1/e of its peak value, where e is the base of natural logarithm. The autocorrelation function of a complex sequence $\{s_n\}$ was computed by:

$$a_k = \frac{\sum_{n=0}^{N-1} s_n \, s_{n+k}^*}{\sum_{n=0}^{N-1} s_n \, s_n^*} \qquad (1)$$

where * denotes the complex conjugate.

Since there could be ground–clutter breakthrough from the antenna sidelobes, the sample mean of the time series was first removed before correlation was performed. This process effectively removed any ground–clutter component from the data.

(c) Estimation of Sea–Clutter Coefficient

The sea–clutter coefficient of a resolution cell is defined as:

$$\sigma^0 = \sigma / A \qquad (2)$$

where σ is the equivalent radar cross section of the sea–clutter return from that cell, and A is the area of the resolution cell given by

$$A = R\theta \frac{c\tau}{2} \sec\phi \qquad (3)$$

where R is the range, θ is the azimuthal beamwidth, c is the velocity of light, τ is the pulse length and ϕ is the depression angle.

High Clutter–to–Noise Ratio(CNR) Case

For data with high CNR, the equivalent sea–clutter RCS is computed by noncoherent integration:

$$\sigma = \frac{1}{N} \sum_{i=1}^{N} (x_i^2 + y_i^2) \qquad (4)$$

where x_i and y_i are the in–phase and quadrature–phase samples of the sea clutter, and N is the number of samples.

Low CNR Case

From spectral analyses of the North Truro sea–clutter data, we found that horizontally polarized sea clutter at L–band and lower was orders of magnitude lower than that for vertical polarization. This made the use of noncoherent integration for determining clutter coefficient unacceptable since the data are dominated by noise. To remedy this problem, σ for the low CNR case was determined using the following steps:

(i) Compute the sea–clutter spectrum from the data;

(ii) Determine the Doppler interval in which the sea clutter spectrum lies(regions where sea–clutter spectral density is greater than the noise density);

(iii) Obtain σ by summing the components of the spectrum over the Doppler interval determined in (ii).

The elevation beamwidths of the X– and S–band antenna were fairly narrow (about 3.5° for X–band and 4.7° for S–band, one–way), resulting in an attenuation of returns from close ranges. For example, at a range of 2 km, the depression angle is about 2.2°. The S–band elevation gain is down approximately 3 dB at this angle. As a result, S–band sea clutter returns at this range will suffer an attenuation of close to 6 dB (two–way). In calculating σ for X–, S–bands, the values were compensated for by adding the amount in dB equal to the negative of the two–way elevation gain of the antenna at the depression angle for that cell.

3. ANALYSIS RESULTS

3.1 Spectral Analysis

Figures 2a and 2b show the sea–clutter spectra for two X–band experiments, for vertical and horizontal polarizations, respectively. Experimental parameters are shown on the figures. Values of SWH and SP during the experiment are also indicated. The spectral resolution is $\Delta = 500/1024 = 0.488$ Hertz per sample. In both cases, the spectra were obtained at a range of 4150 m in three look directions (30°, 75° and 120° azimuth). The Doppler shifts of the sea–clutter spectra were estimated to be –40 Hz (30°), 30 Hz(75°) and 50 Hz(120°) for the V–POL experiment and 0 Hz(30°), 70 Hz(75°) and 90 Hz(120°) for the H–POL experiment.

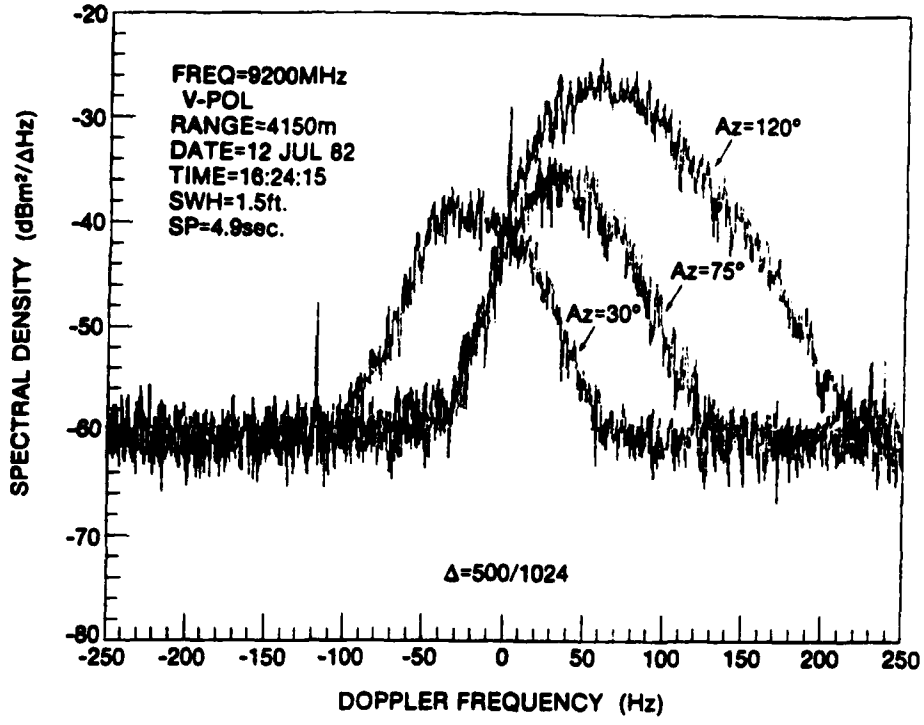

(a) V–POL

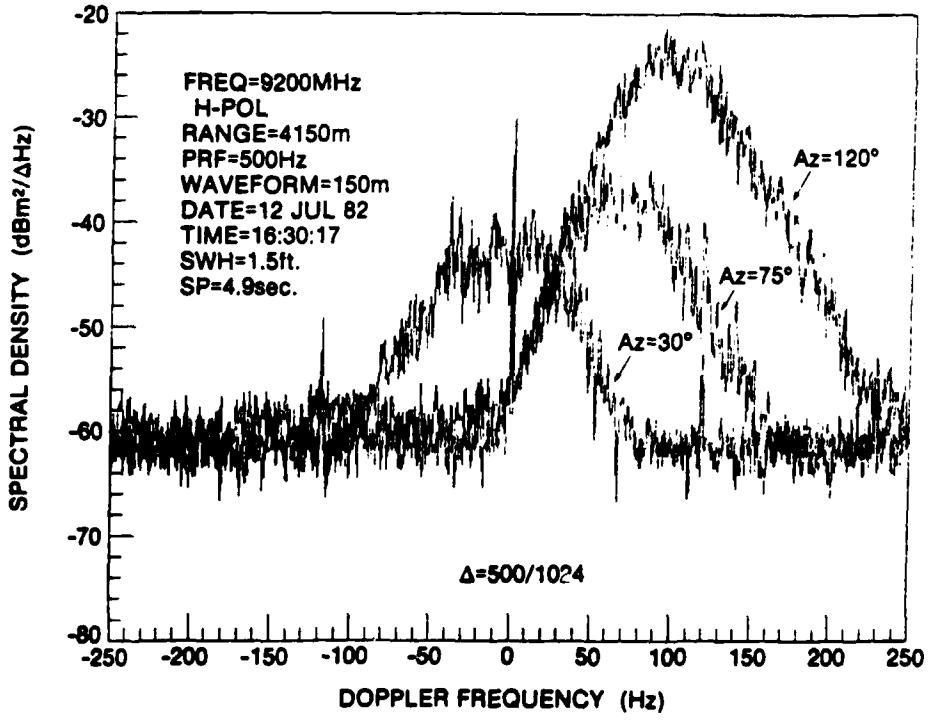

(b) H–POL

Figure 2. Typical low-resolution X–band sea–clutter spectra in the up–swell and near–cross–swell directions.

The spectral power was substantially greater for the spectrum of the 120° azimuth than those of the other two azimuths. The recorded wind speed for these experiments was 7 knots from the direction of 220°. This did not correspond to the direction of the maximum Doppler shift in the sea–clutter spectra. There was no consistent correlation between the recorded wind direction and the direction of maximum Doppler shift in the sea clutter throughout the experiment period. Since ocean current is known to be present in the Cape Cod area, it may be inferred that the observed Doppler shift in the sea clutter was at least partly the result of ocean current. For lack of a more appropriate description, we called the direction with the maximum positive Doppler shift the up–swell (look direction against the sea wave) direction and the direction with near zero Doppler shift in the sea–clutter spectrum the cross–swell (look direction perpendicular to the wave) direction. This result indicated that the up–swell/cross–swell ratio of sea clutter was high at X–band.

The horizontal polarization experiment (Figure 2b) was performed about 5 minutes after the vertical polarization experiment. Consequently, the sea conditions should have been quite similar. We see that the Doppler shift for a horizontal–polarization sea–clutter spectrum was greater than that for vertical polarization for similar sea conditions.

Pidgeon [11] reports this phenomenon and gives a probable explanation. He attributes the difference in the mean Doppler shift between the two polarizations to the different effect of (i) the orbital velocity of the waves and (ii) wind speed have on different polarized radar signals . Since we did not have a precise measurement of the wind velocity at the location where data were collected, it was not possible to verify Pidgeon's theory. More research is needed to explain the mechanisms which produced this difference in Doppler shifts between the two polarizations.

We obtained similar results for S–band with a reduced clutter strength compared to X–band. Figure 3a and 3b show the spectra for two S–band experiments for vertical and horizontal polarization, respectively. These experiments were performed a few minutes before the X–band experiments described earlier. The spectra were computed from data taken from the same general areas as those described in Figure 2. Again we can see that the Doppler shifts in the sea–clutter spectrum for the H–POL data were greater than those for the V–POL data. In Section 3.6.3 we shall present some result which could give some clues to this phenomenon.

Generally, we observed an asymmetrical sea–clutter spectrum, with a longer spectral tail in the direction of the Doppler shift. Symmetrical spectra were observed occasionally in cross–swell conditions where the Doppler shift was near zero. There was no noticeable difference between sea–clutter spectra for high– (15 m) and low–resolution (150 m) waveforms.

Different spectral results were obtained for L–band, UHF and VHF. Figure 4 shows the spectrum of an L–band, V–POL experiment. There were two distinct peaks separated by a Doppler frequency of about 8 Hz. The larger peak was at about +6 Hz, while the other, about 13 dB lower, was at –2 Hz.

In Figure 5 we show the spectra of the L–band, V–POL sea clutter at a fixed range for five look directions. The experimental parameters are shown in the figure. In order to show the separation and the relative magnitude of the spectral peaks clearly, the spectra were offset by 15 dB from one another. That is, the magnitude of the spectrum for 0°

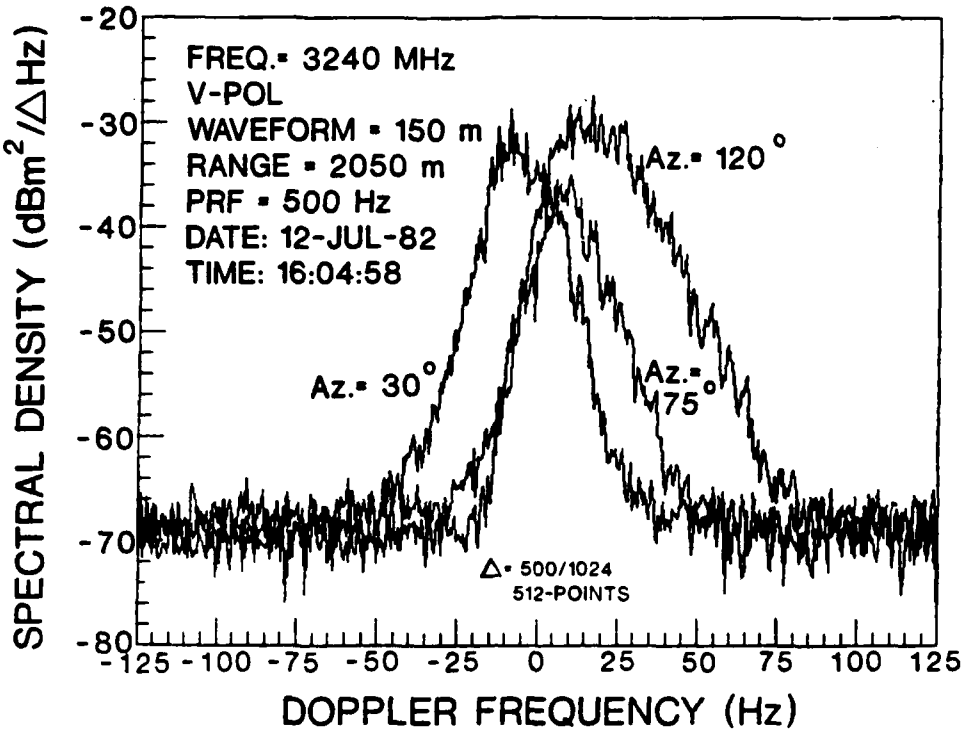

(a) V–POL

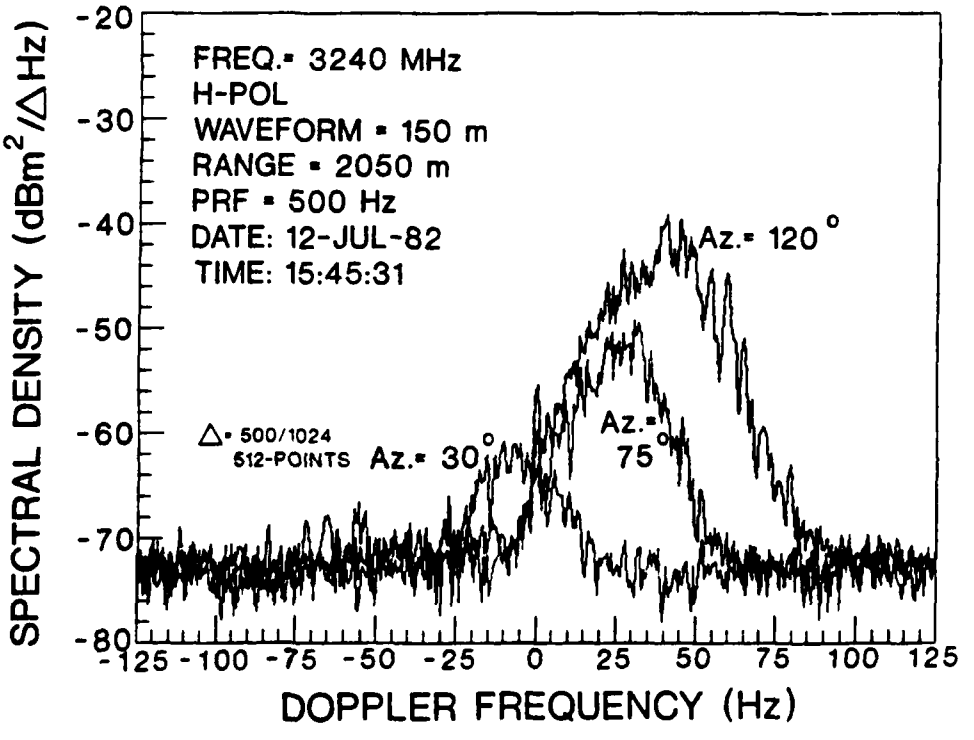

(b) H–POL

Figure 3. Typical low-resolution S–band sea–clutter spectra in the up–swell and near–cross–swell directions.

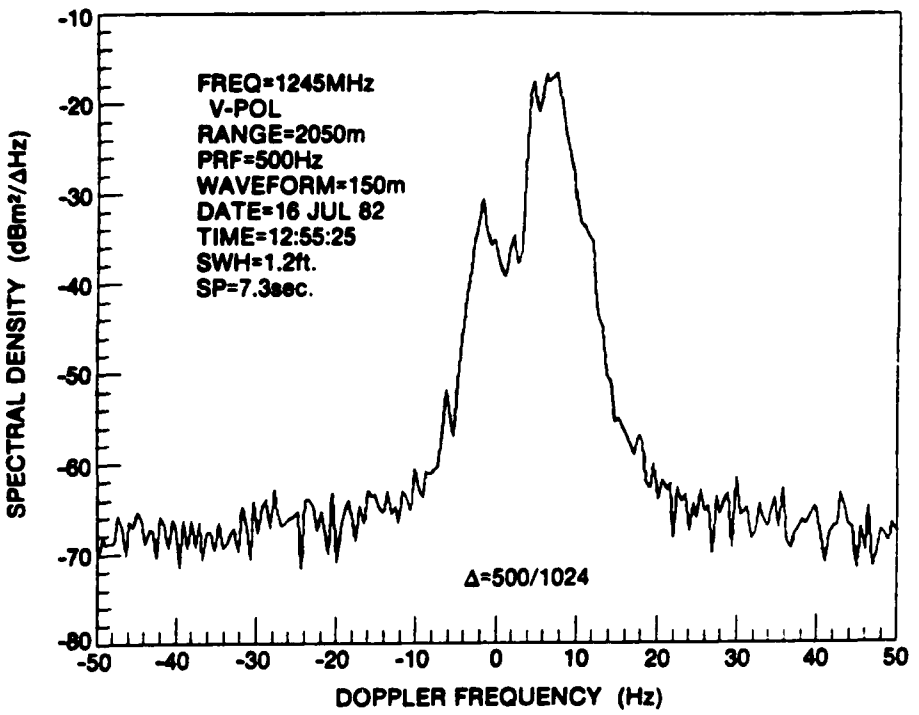

Figure 4. A typical L–band, V–POL low resolution sea–clutter spectrum observed in the up–swell direction.

look direction is correct as appeared in Figure 5, but the spectral magnitudes for look directions of 22.5°, 45°, 67.5° and 90° should be 15 dB, 30 dB, 45 dB and 60 dB higher, respectively, than those shown in the Figure. The spectra have a progressively more positive Doppler shift as the look direction increased from 0° to 90°, indicating that the up–swell direction was near 90°. However, the separation between the two peaks were fairly constant for various look directions. Also in this particular case, the spectral peak having a greater positive Doppler shift had a greater magnitude.

Figure 6 shows the spectra of an L–band, V–POL sea–clutter data set collected from the same general area as those of Figure 5 on a different day. Except for the direction of 90°, the sea–clutter spectra all had double peaks and a negative mean Doppler shift. In this case, however, the spectral peak with a greater negative Doppler shift had a greater magnitude. For the 90° look direction, the sea–clutter spectrum was nearly symmetrical, indicating that this was the cross–swell direction. This condition was seldom observed. Usually, one of the two peaks was substantially higher (15 to 20 dB) than the other Consequently, at longer ranges (> 3 km), the lower spectral peak would be below noise level, leaving only the higher spectral peak visible.

For UHF and VHF, we also observed double peaks in their spectra, as shown in Figure 7 for a VHF experiment. We will briefly discuss the origin of double spectral peaks in Section 3.4.

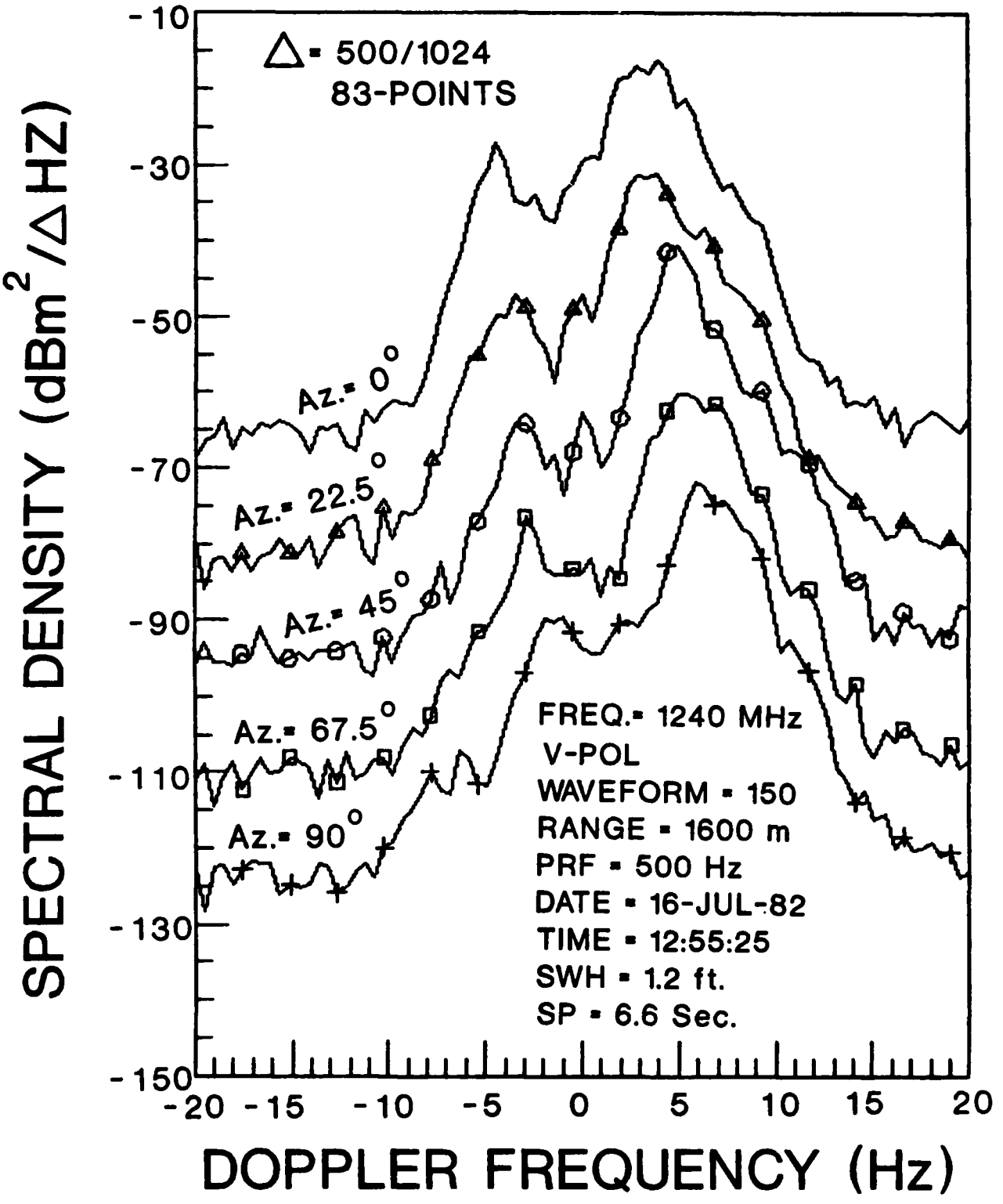

Figure 5 Typical low-resolution L–band, V–POL sea–clutter spectra with positive averaged Doppler shifts.

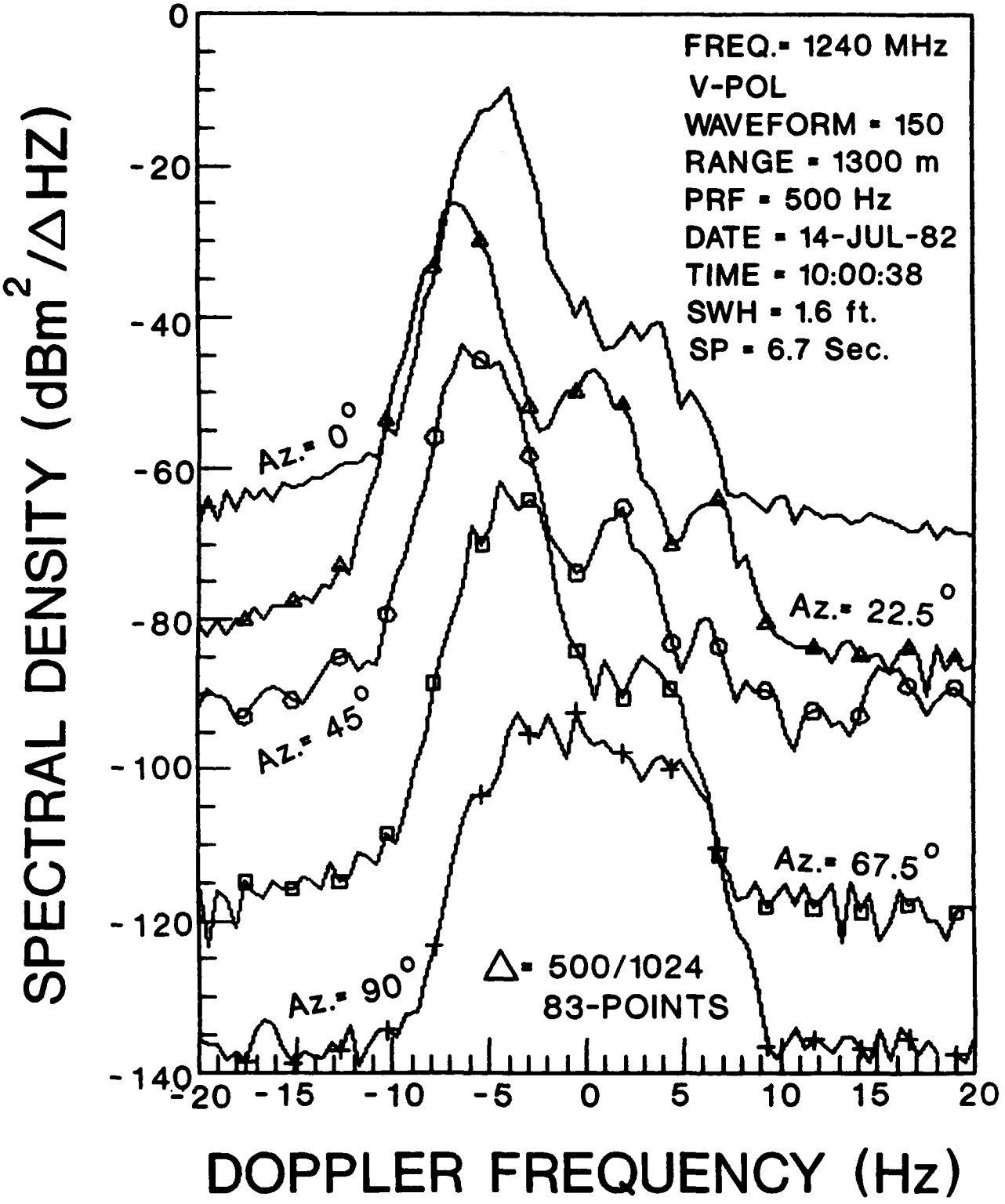

Figure 6. Typical low-resolution L–band sea–clutter spectra with negative averaged Doppler shifts.

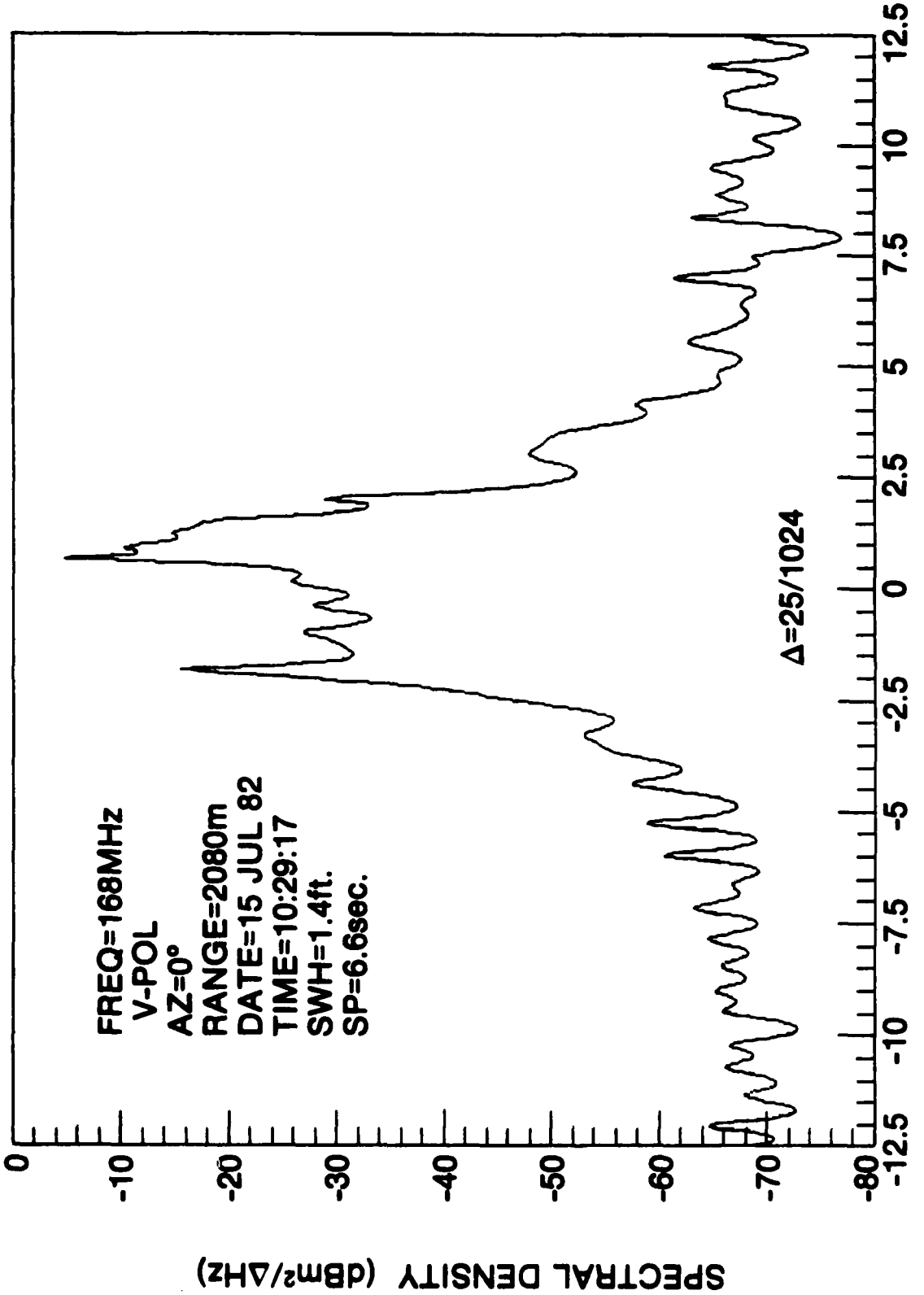

Figure 7. A typical VHF, V–POL sea–clutter spectrum.

3.2 Decorrelation Time Analysis

For a symmetrical spectrum, centred about zero Doppler, the autocorrelation function is a real and even function. If the spectrum has a net Doppler shift, the autocorrelation function is simply the product of the real function (from the zero–Doppler–shift case) with a complex sinusoid, $\exp(\pm j\omega_d T)$, where ω_d is the angular Doppler frequency and T is the time lag. The sign in the complex sinusoid is associated with the direction of the Doppler shift. For a positive Doppler shift, the exponential is $\exp(-j\omega_d T)$, and for a negative Doppler shift, the exponential is $\exp(+j\omega_d T)$. If one has a symmetrical sea–clutter spectrum that can be represented by a Gaussian function, the spectral width and the Doppler shift can be determined from the autocorrelation function. Although in general, sea–clutter spectra are seldom symmetrical, we can obtain a fairly good estimate of the sea–clutter Doppler shift and spectral width using this method.

For X– and S–bands, we found the following empirical relationship works reasonably well: the 3 dB spectral width of the sea–clutter is approximately equal to the inverse of twice the decorrelation time.

Figures 8a and 8b show the spectrum and the autocorrelation function, respectively, of the S–band sea–clutter from a resolution cell. In Figure 8a we superimposed a smoothed curve (using a 10–point block averaging) to enable us to determine the Doppler shift and the 3 dB spectral width, which we estimated to be 17 Hz and 23 Hz respectively. In Figure 8b we estimated the decorrelation time to be 22 msec. Using the empirical relationship given in the preceding paragraph, we obtain a 3 dB spectral width of 22.7 Hz. The period of the modulating sinusoid for the autocorrelation function was determined from the distance of the second zero–crossing of the imaginary part from the origin. The imaginary part of the autocorrelation function started at zero, and the point of the second zero–crossing represented a full period. We estimated the period from Figure 8b to be about 53.5 msec. This gave an estimated Doppler shift of 18.8 Hz. These figures agreed fairly well with the spectrum shown in Figure 8a.

Typical decorrelation times for X–, S–bands were 10 msec and 30 msec, respectively, over most of the experiments. Decorrelation time analysis is less meaningful for lower frequencies owing to the presence of double peaks in their spectra. In this case the autocorrelation function provides information only on the larger spectral peak.

3.3 Clutter Coefficient as a Function of Grazing Angle

Figure 9 shows the σ^o vs grazing angle profiles for the X–band data whose spectra are compared in Figure 2a and 2b. The Doppler shifts typical of the sea–clutter are indicated for each look direction. For both vertical and horizontal polarizations, σ^o was substantially higher in directions of positive Doppler shift. The magnitudes of σ^o were similar for both polarizations in the same look direction. The 120° azimuth and the 30° azimuth were identified as the up–swell and cross–swell directions based on the estimated Doppler shifts in their respective spectra. Generally, σ^o decreased as the look direction moved away from the up–swell direction. We did not observe further decrease in σ^o for directions with negative Doppler shifts in the spectra.

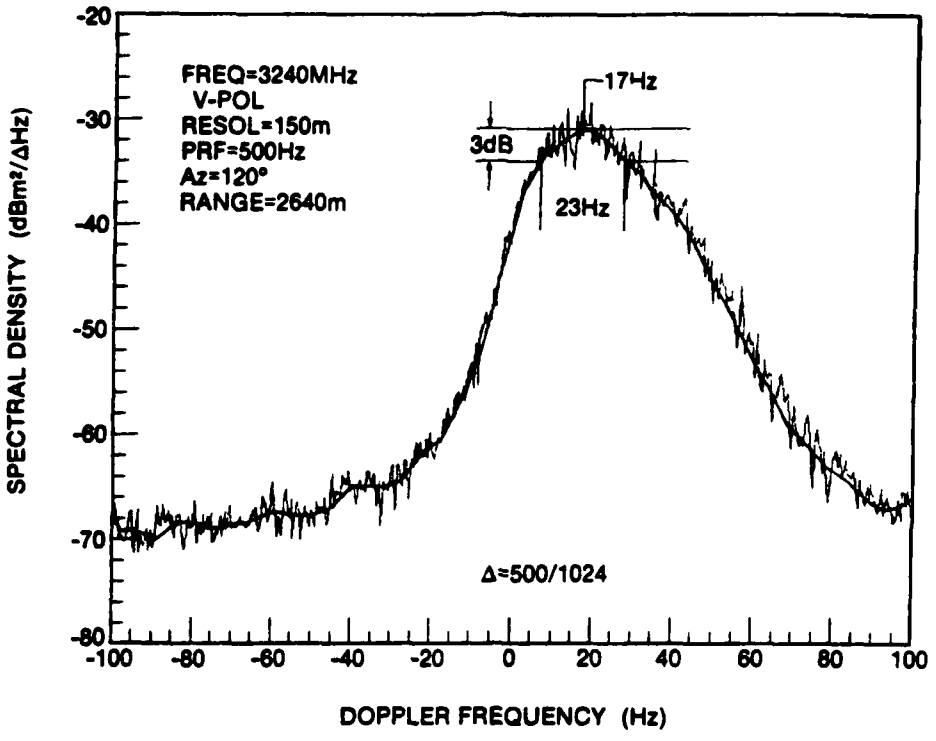

(a) Spectrum

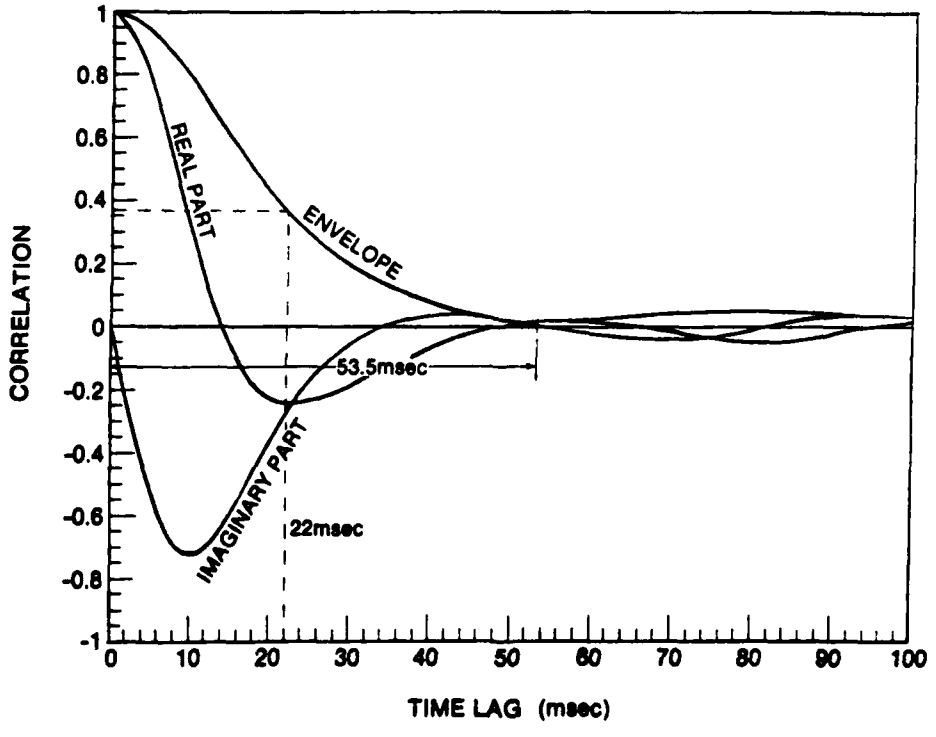

(b) Autocorrelation function.

Figure 8. Relationship between sea–clutter spectrum and autocorrelation.

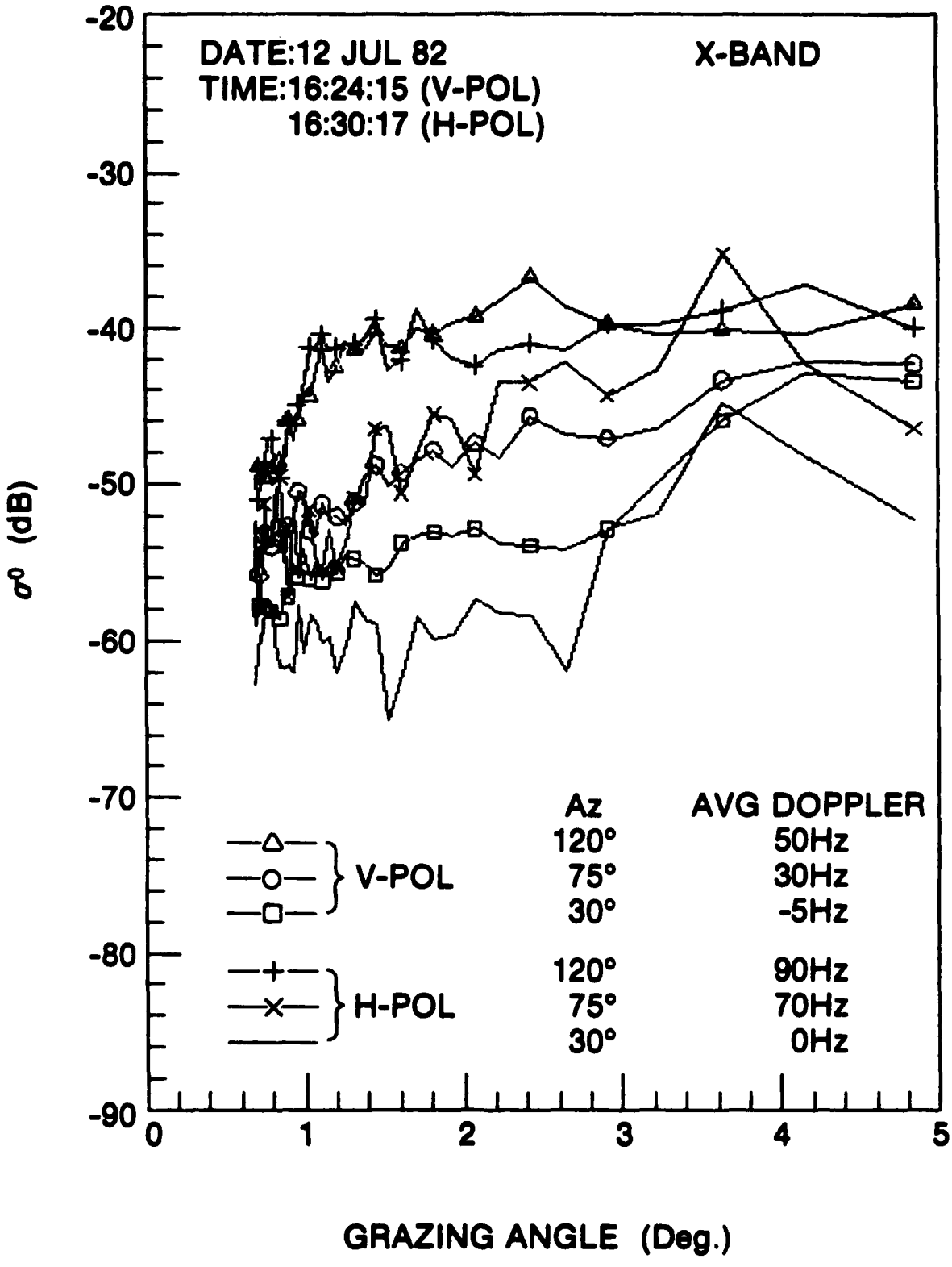

Figure 9. Typical σ^{o} vs. grazing angle profiles of X–band sea clutter in various look directions.

We obtained similar results for S–band, as shown in Figure 10. This S–band experiment was performed approximately 10 minutes before those of the X–band experiments described in the preceding section. The S–band σ^o was approximately 10 dB lower than the corresponding X–band values for the same look direction. The vertical–to–horizontal ratio of σ^o was also higher for S–band than for the X–band. The exact value, however was dependent on the look direction with respect to that of the sea waves.

A different characteristic was observed for L–band. In Figure 11, we show the σ^o vs. grazing angle profiles for two L–band experiments, one V–POL and one H–POL. In both cases, the look directions were 0°, 22.5°, 45°, 67.5° and 90°. The representative Doppler shift for the sea clutter in each look direction ranged from 3 Hz (0°) to about 7 Hz (90°). The σ^o vs grazing angle profiles for all five look directions were very similar. For horizontal polarization, the σ^o values were very low (about –70 dB at 4° grazing angle). The anomalous peaks in the σ^o vs grazing angle profile were due to targets of opportunity (boats) whose Doppler fell within the clutter region, and the rising trend for grazing angles below 1.7° was due to receiver noise.

In Figure 12 we show the σ^o vs grazing angle profiles for an L–band experiment performed on a different day. Here, the Doppler shifts of the spectra in all directions were negative. Comparing Figures 11 and 12, we found that values of σ^o were similar for L–band sea clutter with either positive or negative Doppler shifts, except for negative Doppler shifts near zero. This implied that the up–swell/down–swell ratio of σ^o was close to unity, and the up–swell/cross–swell ratio of σ^o was moderately high for L–band (about 10 dB from Figure 12). The vertical–to–horizontal ratio of σ^o was very large at L–band.

We obtained similar results for UHF and VHF. Figure 13 shows a typical σ^o vs grazing angle profile for VHF sea clutter. In the UHF case, only vertical–polarization data were available.

3.4 Comparison with Established Sea–Clutter Models

A number of sea–clutter models are available to predict σ^o, and they provide fairly reliable σ^o estimates at high grazing angles (above 10°). However, considerable disagreement exists among some of the sea–clutter models at low grazing angles and at low sea states. The Georgia Institute of Technology (GIT) sea–clutter model[12] provides prediction of sea–clutter σ^o from 1 GHz to 100 GHz. The Sittrop model[13] is derived from experimental data at X–band and Ku band. To date, the data for UHF and VHF are insufficient to develop comprehensive models.

As discussed earlier, the North Truro data might include effects of ocean currents which the GIT and the Sittrop models do not address. Instead these models employ the look direction with respect to the wind direction as an input parameter. There is no assurance that sea clutter observed in the presence of ocean current will be similar to that observed from a wind driven sea surface. Consequently, a direct comparison between the North Truro results with these models was not possible. Nevertheless, it would be qualitatively informative to compare the North Truro results with predictions obtained from the above mentioned models assuming similar sea conditions. The reasoning was that, in an open ocean, a sea wave travelling in a given direction could be a result of a steady wind blowing in the same direction.

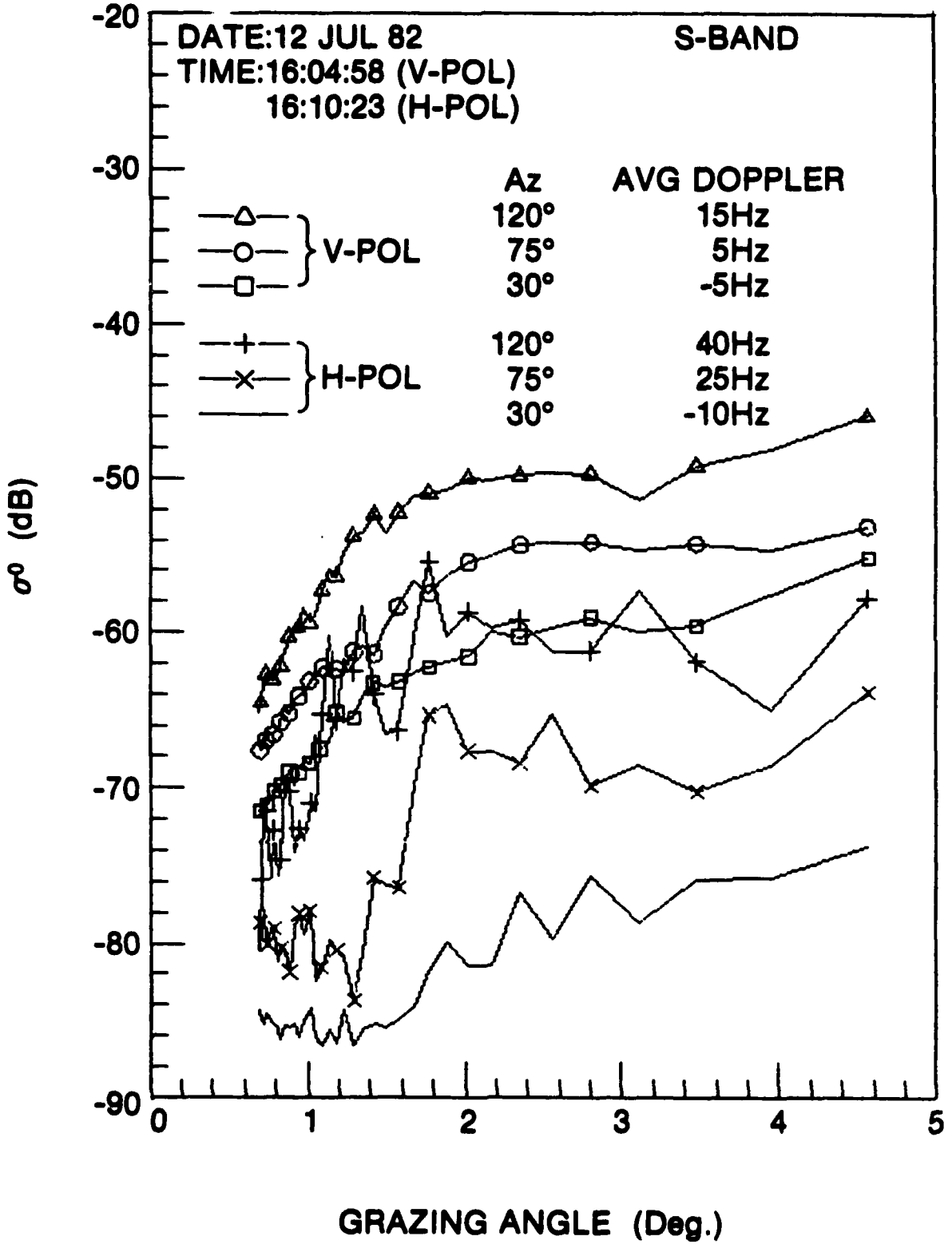

Figure 10 Typical σ° vs. grazing angle profiles of S–band sea clutter in various look directions.

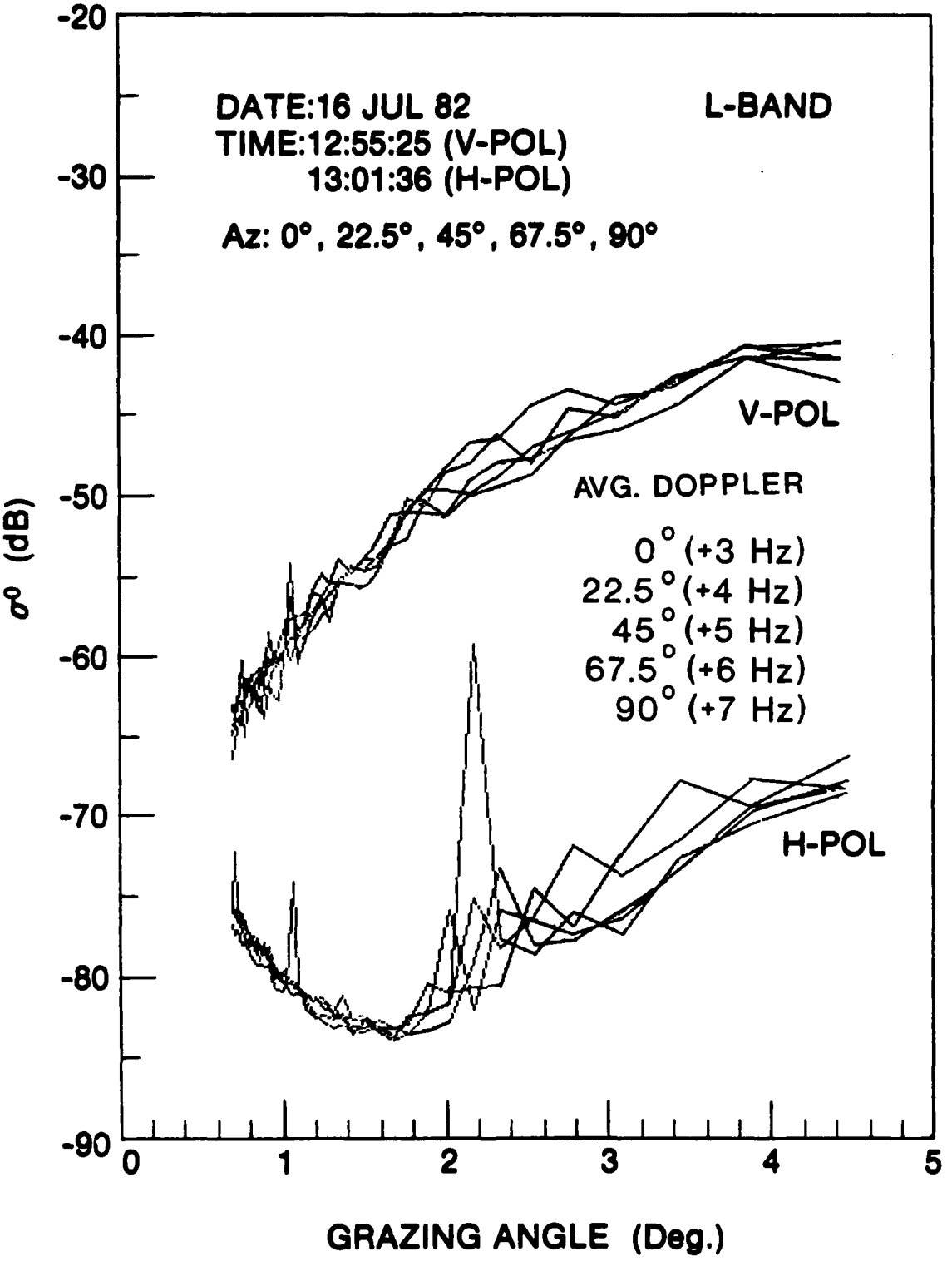

Figure 11 Typical σ^{o} vs. grazing angle profiles of L–band sea clutter in various look directions from up–swell.

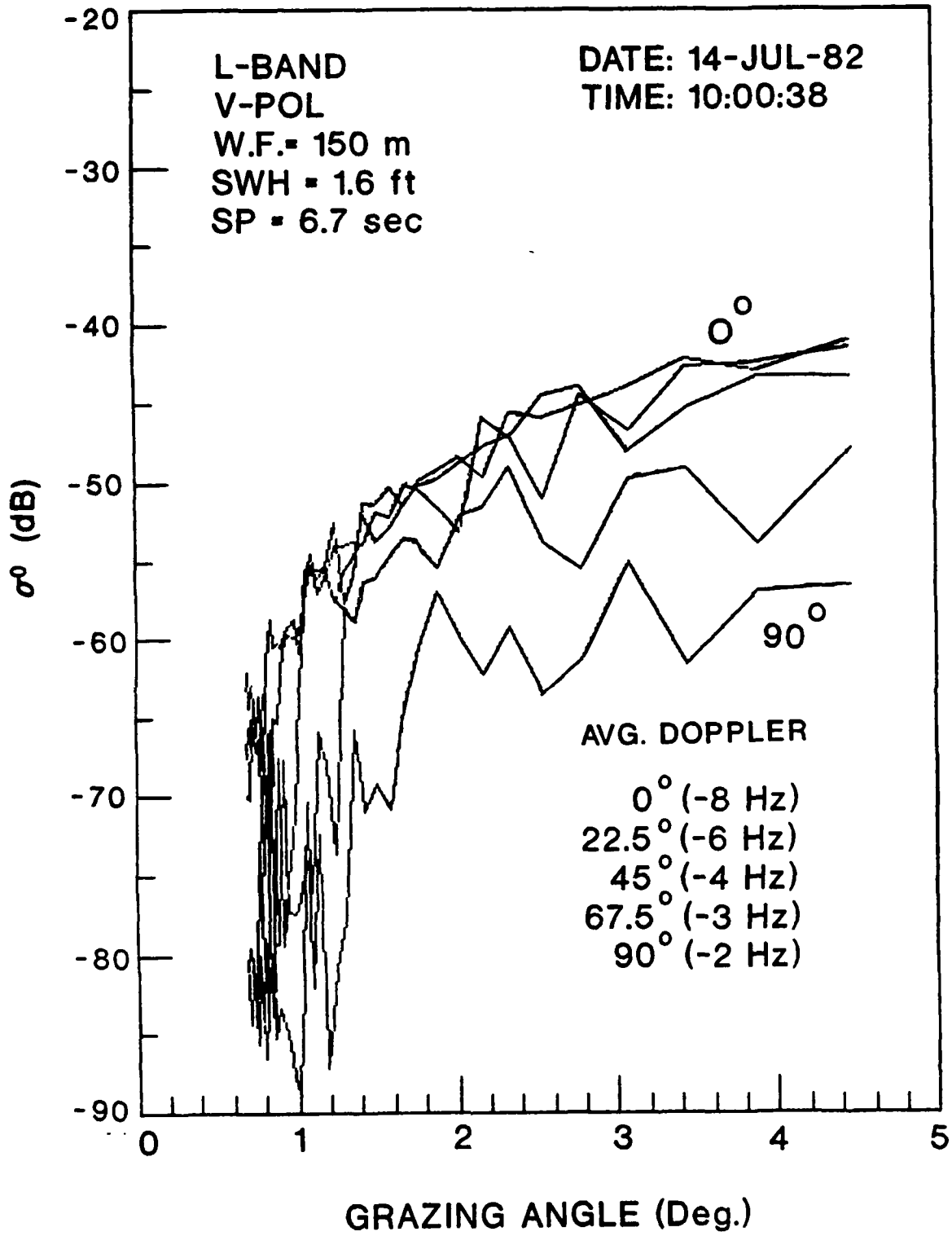

Figure 12 Typical σ^{o} vs. grazing angle profiles of L–band sea clutter in various look directions from down–swell.

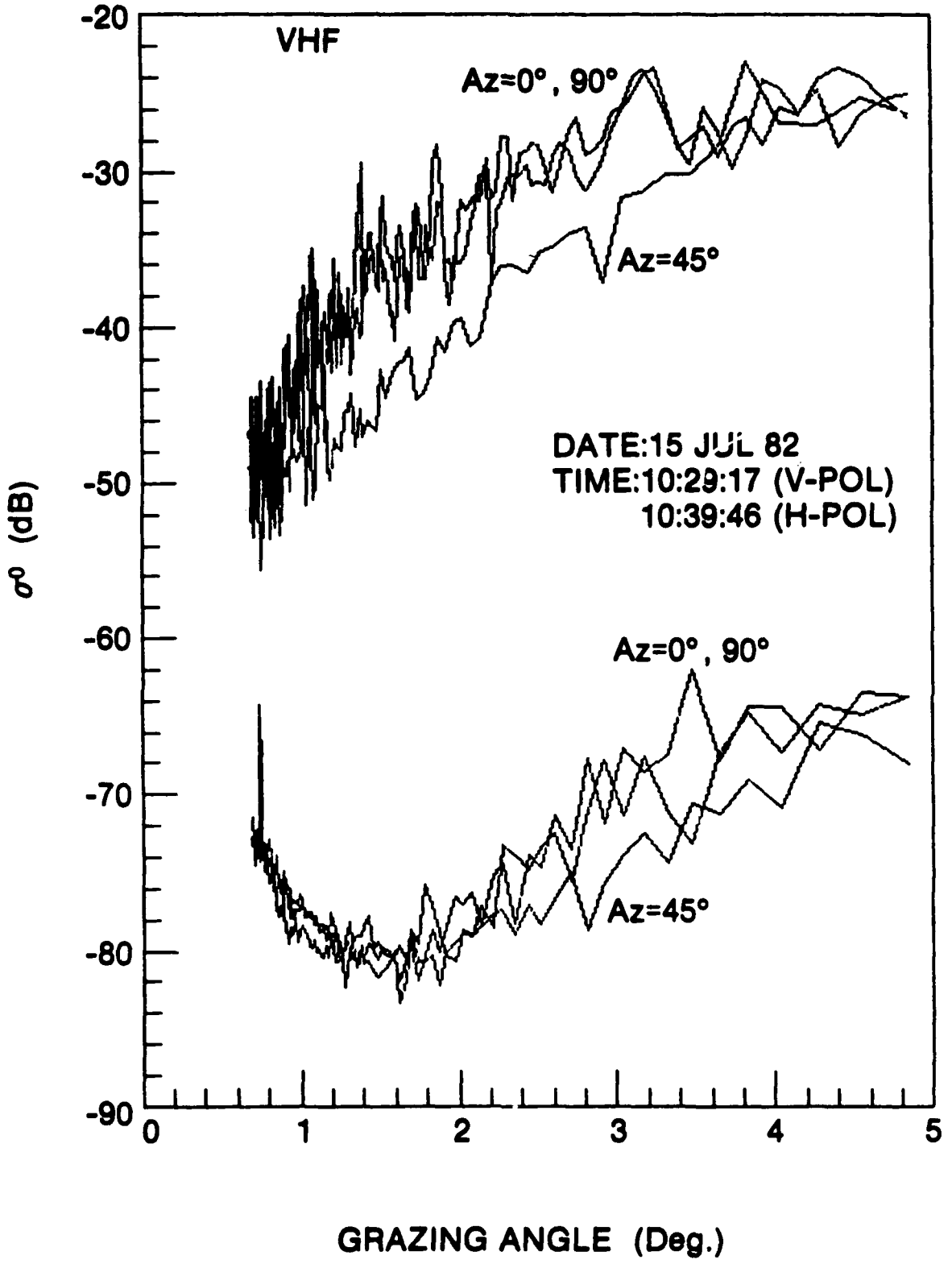

Figure 13 Typical σ^{o} vs. grazing angle profiles for VHF sea clutter in various look directions.

In Figure 14, we plotted the North Truro X–band σ^o vs grazing angle profiles together with those predicted by the GIT and the Sittrop models. For the GIT model, we used an average wave height of 0.2 m, and for the Sittrop model, we used a sea state value of 2. In the range of grazing angles from 1.5° to 5°, we found a reasonably good agreement between the North Truro X–band data (up–swell condition) and the GIT model (upwind condition). The match was less good for grazing angle below 1°. Also the GIT model predicted a much smaller upwind–to–crosswind σ^o ratio than the North Truro up–swell/cross–swell σ^o ratio. The Sittrop model yielded reasonably close results for grazing angles above 3° and below 0.5°. Also its cross–wind results matched the North Truro cross–swell results closer than did the GIT model. However considerable discrepancy was found in the range of grazing angle between 0.5° and 3°.

Results for S– and L–bands are shown in Figures 15 and 16, respectively. Only the GIT model was used in comparison.

Profiles of σ^o vs grazing angle for UHF and VHF sea clutter are given in Figure 17. These profiles were very consistent over the two–week period. There were no H–POL data for UHF.

There was a much greater variability in σ^o at low grazing angles($< 2^o$) than at higher grazing angles. To show how σ^o varied with radar frequency in the low grazing angle region, we plotted in Figure 18 the σ^o values for various bands at a grazing angle of 2°. The corresponding V–POL/H–POL σ^o ratio were also shown.

Examining Figures 14 to 18, we noted the following:

(i) V–POL σ^o for X–, S– and L–bands were similar except in the up–swell direction where the X–band values were about 10 dB higher;

(ii) V–POL/H–POL ratio of σ^o increased with decreasing frequency;

(iii) σ^o increased as frequency decreased below L–band.

The above results together with the spectral–analysis results reinforced the theory that the main mechanisms contributing to sea clutter are (a) surface effects such as water sprays and droplets, (b) wave facets and (c) Bragg resonance.

The surface effects affected mainly the X–band and to a lesser extent, S–band. This could account for the high σ^o values at X–band compared to those of the S– and L–bands and the relatively low V–POL/H–POL ratio. Scattering of X–band signals by water droplet occurs in the upper portion (relative to those of S– and L–bands) of the Rayleigh region and will produce a much stronger return than at S– and L–bands. The spherical shape of water droplets means that both V–POL and H–POL signals were scattered equally well.

Rayleigh scattering predicts an effective RCS proportional to $1/\lambda^4$ where λ is the radar wavelength. However, the measured σ^o values for S– and L–bands did not follow this relationship. Scattering of microwave from small wave facets of capillary waves may account for the less rapid rate of decrease of effective RCS with increasing wavelength than predicted by Rayleigh scattering theory.

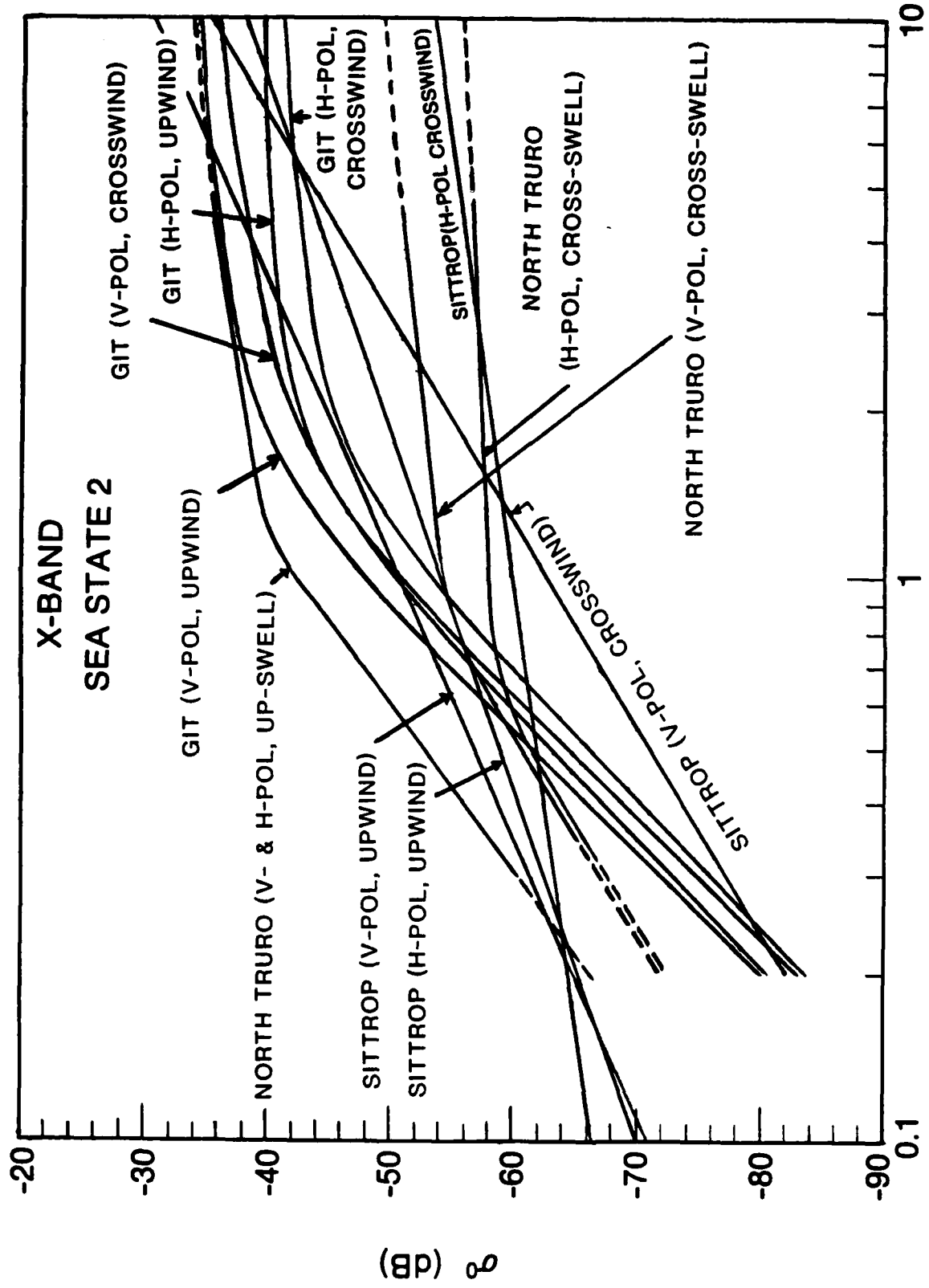

Figure 14 Averaged X-band σ^{o} vs grazing angle profiles for North Truro in the up-swell and cross-swell conditions and those calculated from the GIT and Sittrop models assuming upwind and crosswind conditions.

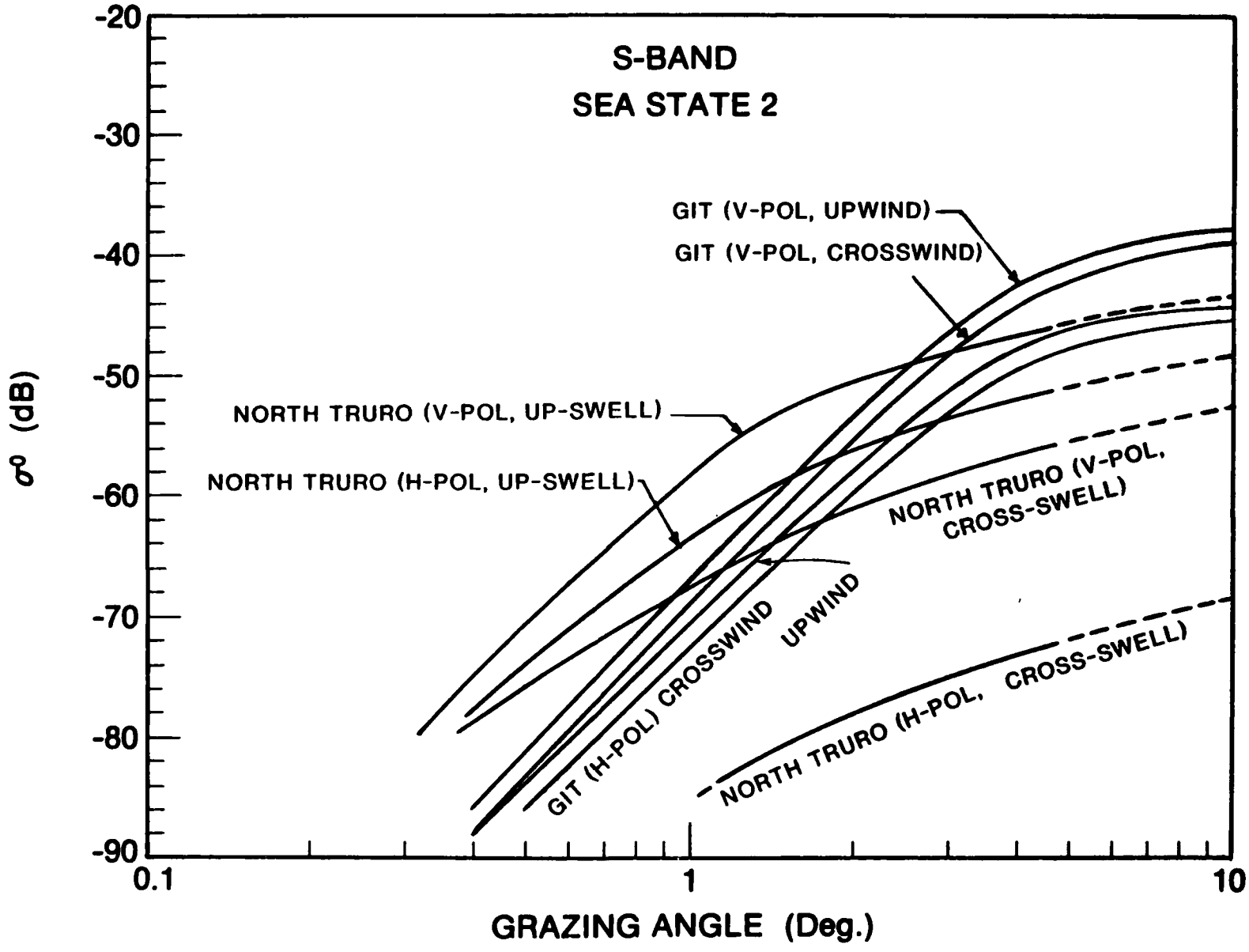

Figure 15 Averaged S-band σ^o vs grazing angle profiles for North Truro in the up-swell and cross-swell conditions and those calculated from the GIT model assuming upwind and crosswind conditions.

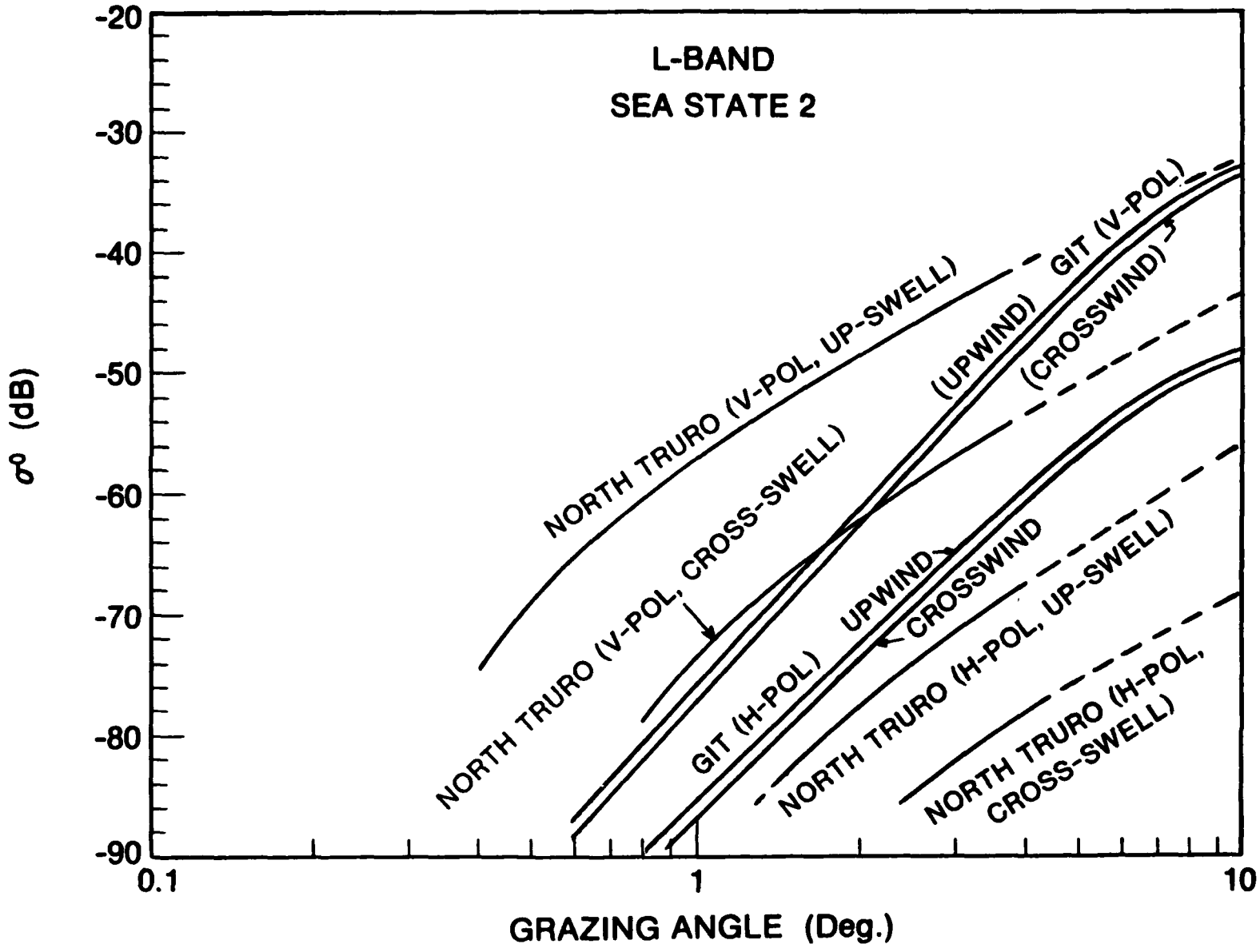

Figure 16 Averaged L-band σ^o vs grazing angle profiles for North Truro in the up-swell and cross-swell conditions and those calculated from the GIT model assuming upwind and crosswind conditions.

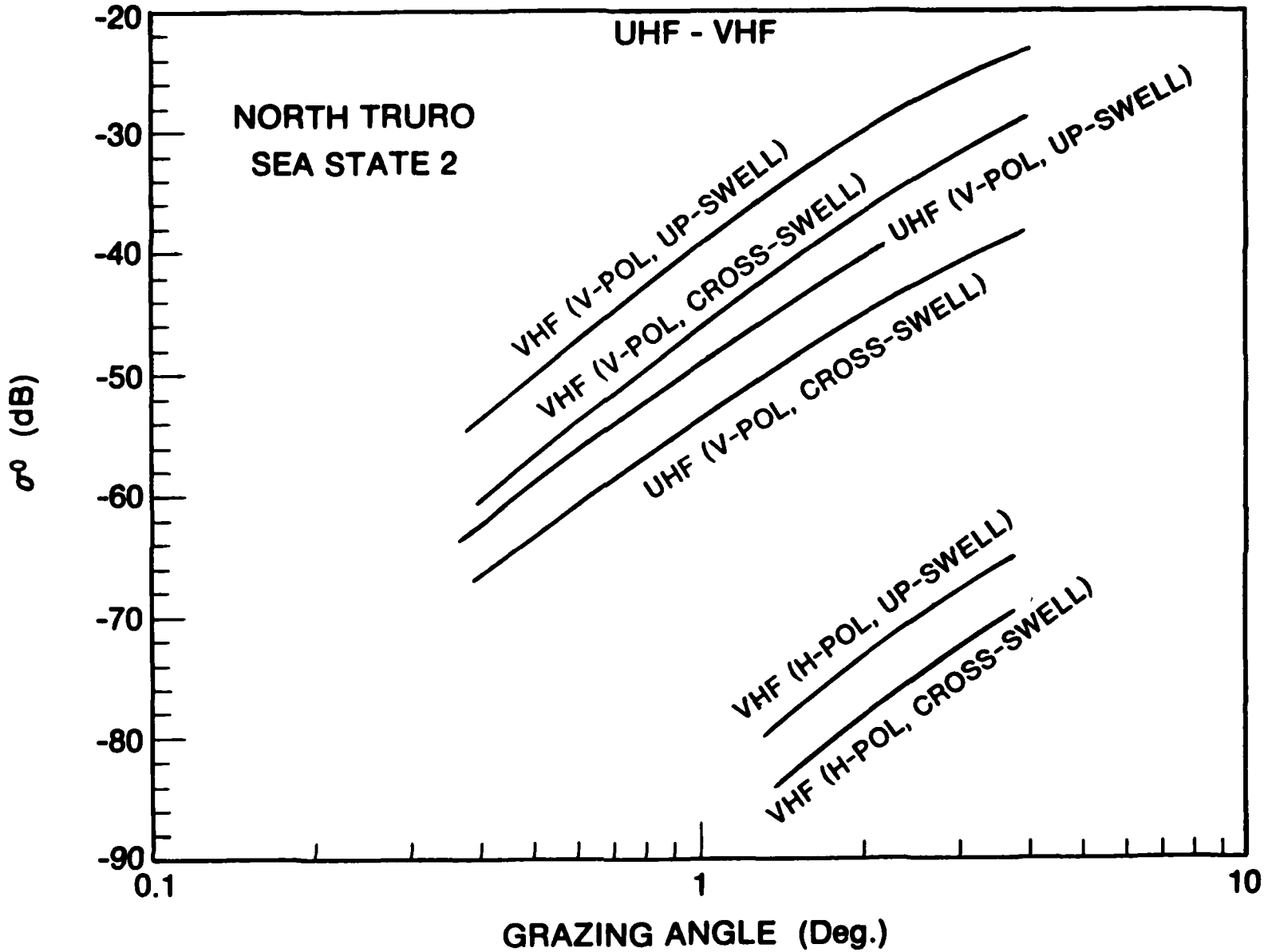

Figure 17 Averaged UHF and VHF σ^o vs grazing angle profiles for North Truro in up-swell and cross-swell conditions.

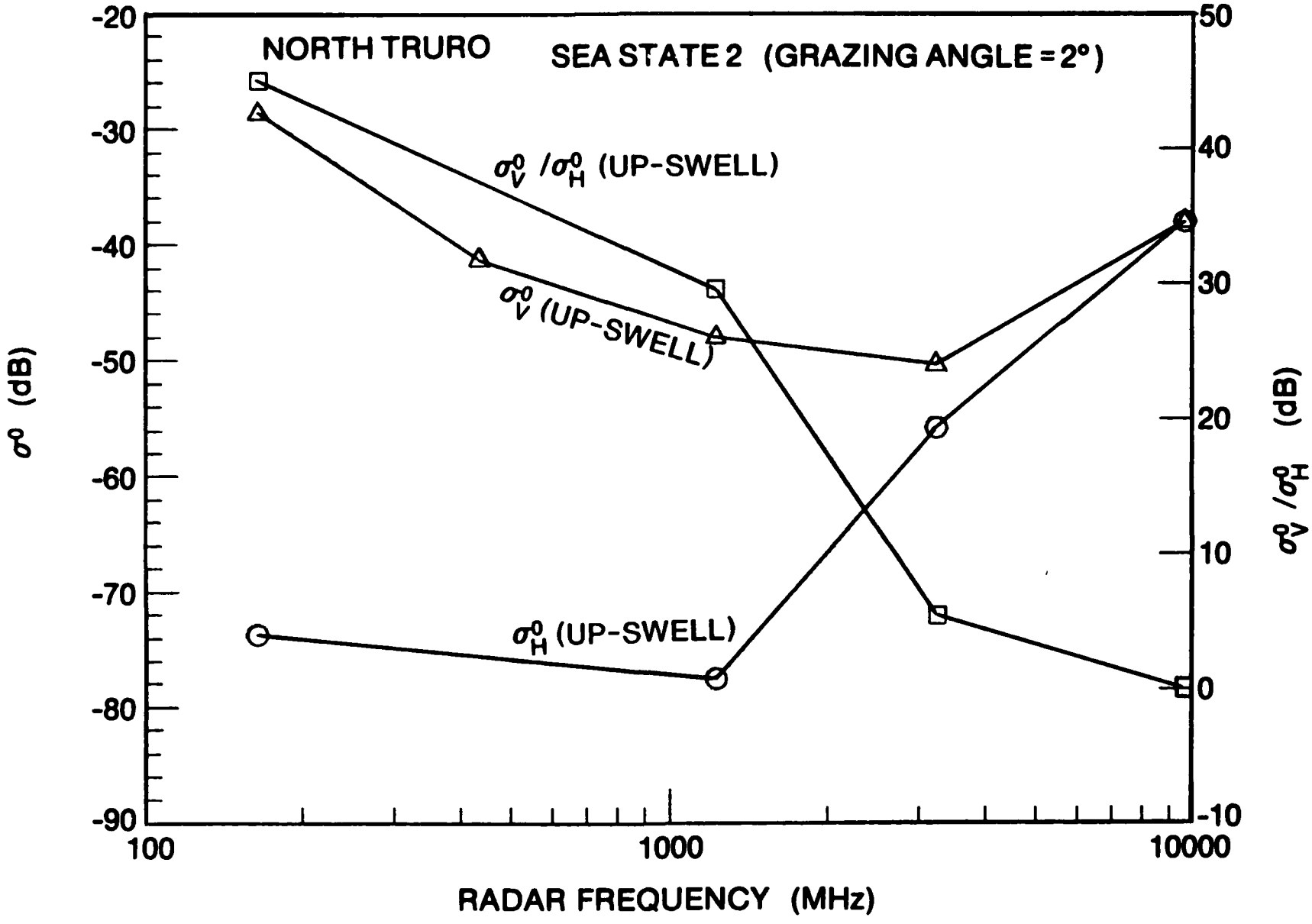

Figure 18 Averaged σ^o and σ_V^0/σ_H^0 as a function of frequency for the North Truro sea-clutter data

A capillary wave is generated by wind, but its velocity of propagation is controlled mainly by surface tension of the water. The wavelength of a capillary wave is measured in terms of centimeters. Scattering from wave facets could occur in the upper portion of the Rayleigh region and the resonance region.

The double peaks exhibited by sea clutter at low frequency bands and the rising σ^o below L–band suggested that a different mechanism was the major contributor of sea clutter at these frequencies. This was attributed to Bragg resonance of surface waves [14]. The Bragg Doppler shifts of sea surface waves at low grazing angles is given approximately by[14]:

$$f_B = \pm \left[\frac{g}{\pi \lambda}\right]^{1/2} \tag{5}$$

where g is the gravitational acceleration (9.8 m/sec^2), and λ is the radar wavelength.

Applying Eqn (5) to the VHF case, we obtained a value of ±1.32 Hz, giving a peak separation of 2.64 Hz, which was in good agreement with the figure observed in Figure 7. Similar agreements were obtained for the L–band and UHF cases.

3.5 Sea–Clutter Amplitude Distribution

Statistical properties of sea clutter are of interest to radar designers for the prediction of probability of detection(P_d) and probability of false alarm(P_{fa}). In this sub–section, results are shown for the relative goodness of fit of sea–clutter amplitude distributions to some elementary statistical models. We considered Rayleigh, Weibull[15], lognormal[16] and the K–distribution[17,18]. The model cumulative distribution function (cdf), probability density function (pdf), and the moments necessary to compute the model parameters are defined in Equations (6) through (20).

Rayleigh

cdf: $$P(x) = 1 - \exp\{-\frac{x^2}{a}\} \qquad 0 \le x \le \infty \tag{6}$$

pdf: $$p(x) = \frac{2x}{a} \exp\{-\frac{x^2}{a}\} \tag{7}$$

First moment: $$\langle x \rangle = \frac{(\pi a)^{1/2}}{2} \tag{8}$$

Weibull

$$\text{cdf:} \qquad P(x) = 1 - \exp\{-\frac{x^n}{a}\} \qquad (9)$$

$$0 \leq x \leq \infty$$

$$\text{pdf:} \qquad p(x) = n\left[\frac{x^{n-1}}{a}\right] \exp\{-\frac{x^n}{a}\} \qquad (10)$$

$$\text{First moment:} \quad \langle x \rangle = a^{1/n}\, \Gamma(1 + \frac{1}{n}) \qquad (11)$$

$$\text{second moment:} \quad \langle x^2 \rangle = a^{2/n}\, \Gamma(1 + \frac{2}{n}) \qquad (12)$$

where $\Gamma(z)$ is the gamma function.

Lognormal

$$\text{cdf:} \qquad P(x) = 1 - \frac{1}{2}\, \text{erfc}(\frac{\ln x - m}{a^{1/2}}) \qquad (13)$$

$$0 \leq x \leq \infty$$

where erfc(z) is the complementary error function.

$$\text{pdf:} \qquad p(x) = \frac{1}{x(\pi a)^{1/2}} \exp\{-\frac{(\ln x - m)^2}{a}\} \qquad (14)$$

$$\text{First moment:} \quad \langle x \rangle = \exp(m + \frac{a}{4}) \qquad (15)$$

$$\text{Second moment:} \quad \langle x^2 \rangle = \exp(2m + a) \qquad (16)$$

K–Distribution

$$\text{cdf:} \qquad P(x) = 1 - \frac{2}{\Gamma(\nu)} \left[\frac{b\,x}{2}\right]^{\nu} K_{\nu}(bx) \qquad (17)$$

$$0 \leq x \leq \infty$$

$$\text{pdf:} \qquad p(x) = \frac{2b}{\Gamma(\nu)} \left[\frac{b\,x}{2}\right]^{\nu} K_{\nu-1}(bx) \qquad (18)$$

where $K_\nu(z)$ is the modified Bessel function of the third kind of order ν.

$$\text{Second moment: } \langle x^2 \rangle = \left[\frac{2}{b}\right]^2 \nu \tag{19}$$

$$\text{Fourth moment: } \langle x^4 \rangle = 2\left[1 + \frac{1}{\nu}\right]\langle x^2 \rangle^2 \tag{20}$$

Note that parameters ν and b of the K–distribution are usually defined in terms of the first and second moments of the clutter RCS which are the second and fourth moments of the clutter amplitude, respectively.

From the radar perspective, standard statistical tests such as the chi–square goodness of fit test [19] are of limited use for clutter data. The reason is that these tests place an equal importance in the goodness of fit on all regions of the probability space. In radar applications, goodness of fit of clutter statistics to a model is important mainly in the low P_{fa} region.

In the standard chi–square goodness of fit test, the pdf of the statistical model is divided into K intervals of equal probability (i.e., 1/K). Parameter χ^2 is defined as:

$$\chi^2 = \sum_{i=1}^{K} \frac{(f_i - \frac{N}{K})^2}{(\frac{N}{K})} \tag{21}$$

where f_i = observed number of occurrences of a clutter sample having an amplitude within the ith interval, and N = total number of amplitude samples forming the histogram. (N/K) is the expected number of occurrences in each interval for the statistical model.

A lower χ^2 value indicates a better fit to a model. To determine the relative goodness of fit of the sea clutter from a group of resolution cells, we arbitrarily assigned a resolution cell number to each cell in the group. The χ^2 value for data from each cell was computed. The results for various models can be plotted as a function of the resolution cell number to give a visual indication of the relative goodness of fit to the models. Alternatively, the ensemble average of χ^2 for a group of resolution cells can be computed for each model and compared to give a quantitative measure of the relative goodness of fit.

We performed the standard chi–square goodness of fit test on a set of X–band, V–POL, 15 m waveform resolution data using a value of K=50. The length of the time series N was 10000. We obtained the following χ^2 values: 3190.2, 2637.4, 807.4, and 7230.6 for the Rayleigh, Weibull, lognormal and the K models, respectively. Thus the standard test suggested that the data for this experiment fitted the lognormal model best and the K–distribution worst. Upon closer examination, it was found that the data fitted the K–distribution poorly primarily in the $P_{fa} > 0.1$ region. Figure 19 compares the P_{fa} vs threshold (V_T) curve for the above data set with those computed from the four models. It is seen that the data fit the K–distribution best in the amplitude region for which the P_{fa} is ≤ 0.1.

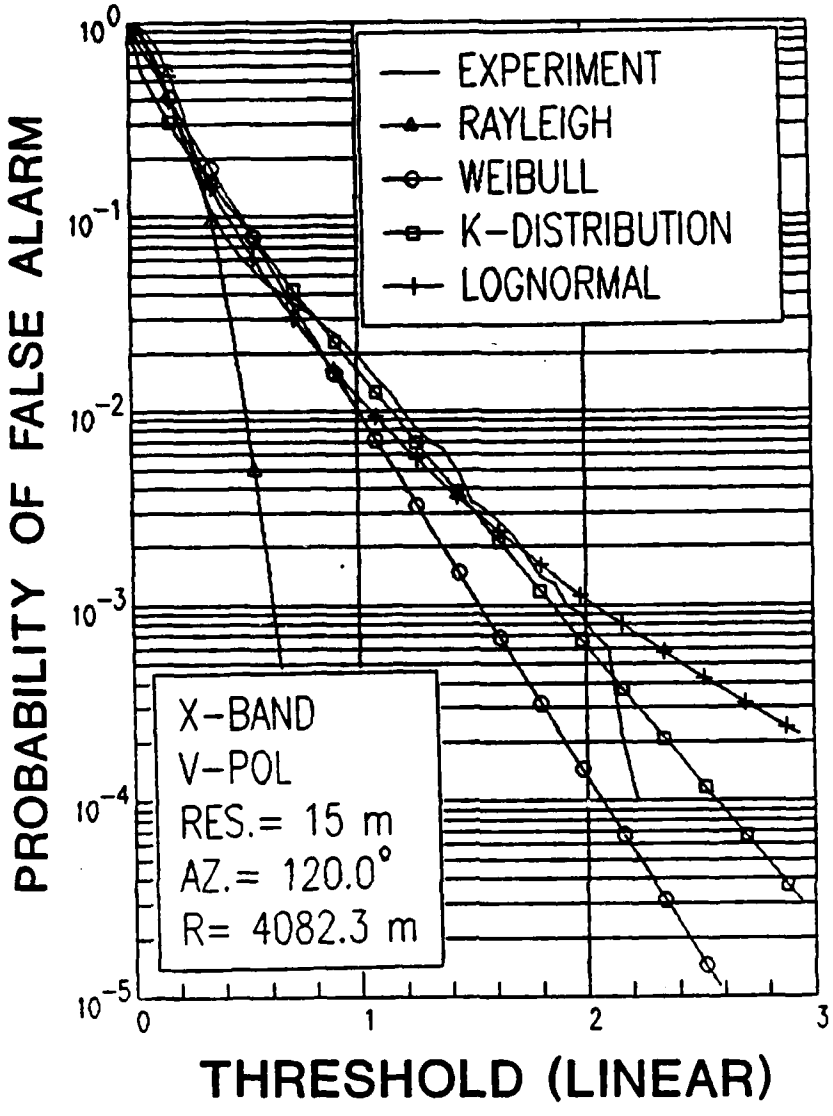

Figure 19 Comparison of the P_{fa} characteristics of an X–band, V–POL sea–clutter data set with those predicted by the Rayleigh, Weibull, lognormal and K models.

Modified Chi–Square Test

To obtain a procedure which brings out the relative merits of various models in the important low P_{fa} region, we modified the chi–square test as follows. Referring to Figure 20, boundaries of equal–probability intervals were determined for each of the statistical models in the amplitude region for which P_{fa} is ≤ 0.1. These boundaries divided this region into K equal–probability intervals, each with a probability of 0.1/K. We defined the modified χ^2 index:

$$\chi_1^2 = \sum_{i=1}^{K} \frac{[f_i - (N\frac{0.1}{K})]^2}{(N\frac{0.1}{K})} \qquad (22)$$

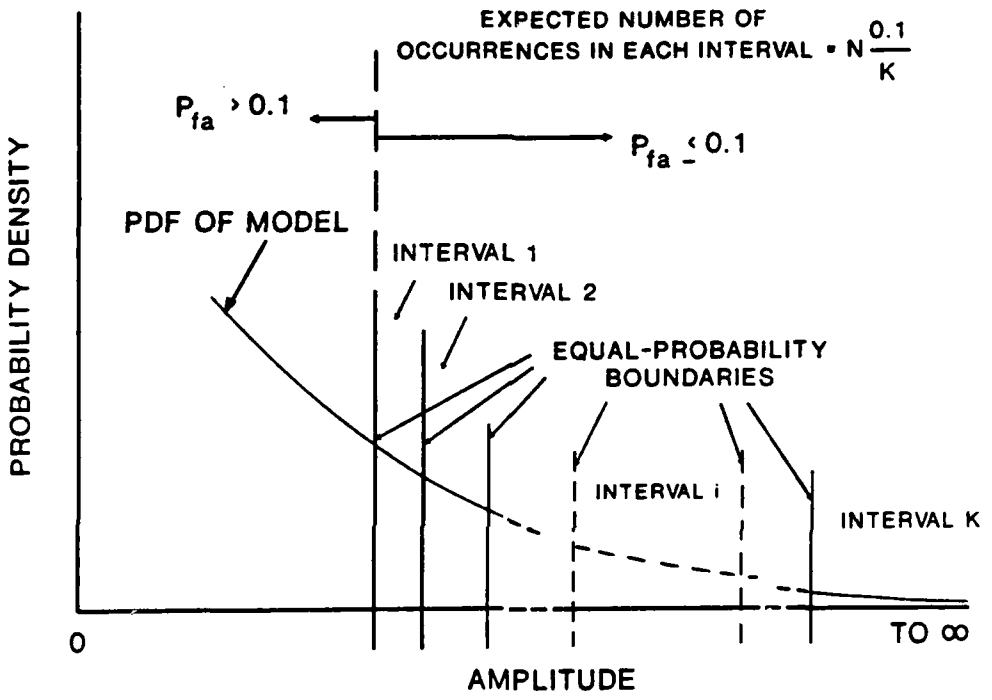

Figure 20 Illustration of the division of equal–probability intervals for the modified chi–square test.

This is equivalent to assigning a zero weighting in the amplitude region where the P_{fa} is greater than 0.1 and a uniform weighting in each of the K intervals. The modified chi–square test is simply a comparison of the χ_1^2 values calculated for each of the statistical models.

Using the modified chi–square test, goodness of fit comparisons were made among sea–clutter data for various combinations of frequency bands (X–, S– and L–band), polarization (V– and H–POL) and waveform resolutions (15m and 150 m). For L–band, H–POL data, the sea–clutter component was very weak, and the composite returns were dominated by receiver noise. Consequently, L–band, H–POL sea–clutter presented a good fit to the Rayleigh and Weibull models.

Figure 21 shows a typical result of the modified chi–square test for low resolution vertical polarization data (X–band, V–POL, 150m waveform). In this figure, the modified chi–square indices for 40 resolution cells are shown. Cell "0" was at a range of 1 km, and each point in the figure represents a range increment of 150 m. There was a number of resolution cells with clutter data having a poor fit to the Rayleigh model, suggesting that non–Rayleigh sea–clutter statistics were common even at low waveform resolutions. On average, these data had the best fit to the Weibull and K–distributions and the worst fit to the lognormal model.

In Figure 22, We plotted the P_{fa} vs V_T curves for data in cell No. 23 of Figure 21. The modified chi–square test showed that this data set had a poor fit to the Rayleigh model and a reasonably good fit to the lognormal model. This was confirmed by the results in Figure 22, and it also showed that the data fitted the K–distribution best.

A typical result of the modified chi–square test for high resolution horizontal polarization data is given in Figure 23 (S–band, H–POL, 15 m waveform). Cell "0" in this figure was 2 km, and each point represents a range increment of 15 m. In this case, the modified chi–square indices for all resolution cells assuming a Rayleigh model were very large (implying a poor Rayleigh fit) and were beyond the scale employed in Figure 23. The data, however, had a reasonably good fit to the lognormal distribution in all resolution cells included in the test.

Figure 24 compares the P_{fa} vs V_T curve for data from a typical resolution cell with those computed from the models. The data fitted the K–distribution best.

To establish the relative merits of the statistical models considered in this study, we computed the ensemble average of the modified chi–square index over a group of resolution cells. We tested data from various combinations of frequency, polarization and waveform resolution. The results are tabulated in Table II.

In nearly all cases, we obtained the best fit of the data to the K–distribution. Generally, the fit to a lognormal distribution improved for high resolution (15m) waveform and for horizontal polarization. The fit to a Rayleigh and Weibull distributions improved for low–resolution waveform (150 m) and vertical polarization.

The results presented in Table II together with those of Figures 21 to 24 indicated the following:

(i) The K–distribution is the most appropriate model for sea clutter in the low P_{fa} region;

(ii) Sea–clutter statistics approached those of a Rayleigh model for low resolution and vertically polarized waveforms;

(iii) Non–Rayleigh sea–clutter statistics were common even for relatively low resolution and vertical polarization waveforms;

(iv) The Weibull distribution was also a good model for low–resolution sea clutter.

(v) Sea–clutter statistics approached those of a lognormal model for high resolution and horizontal polarization waveforms.

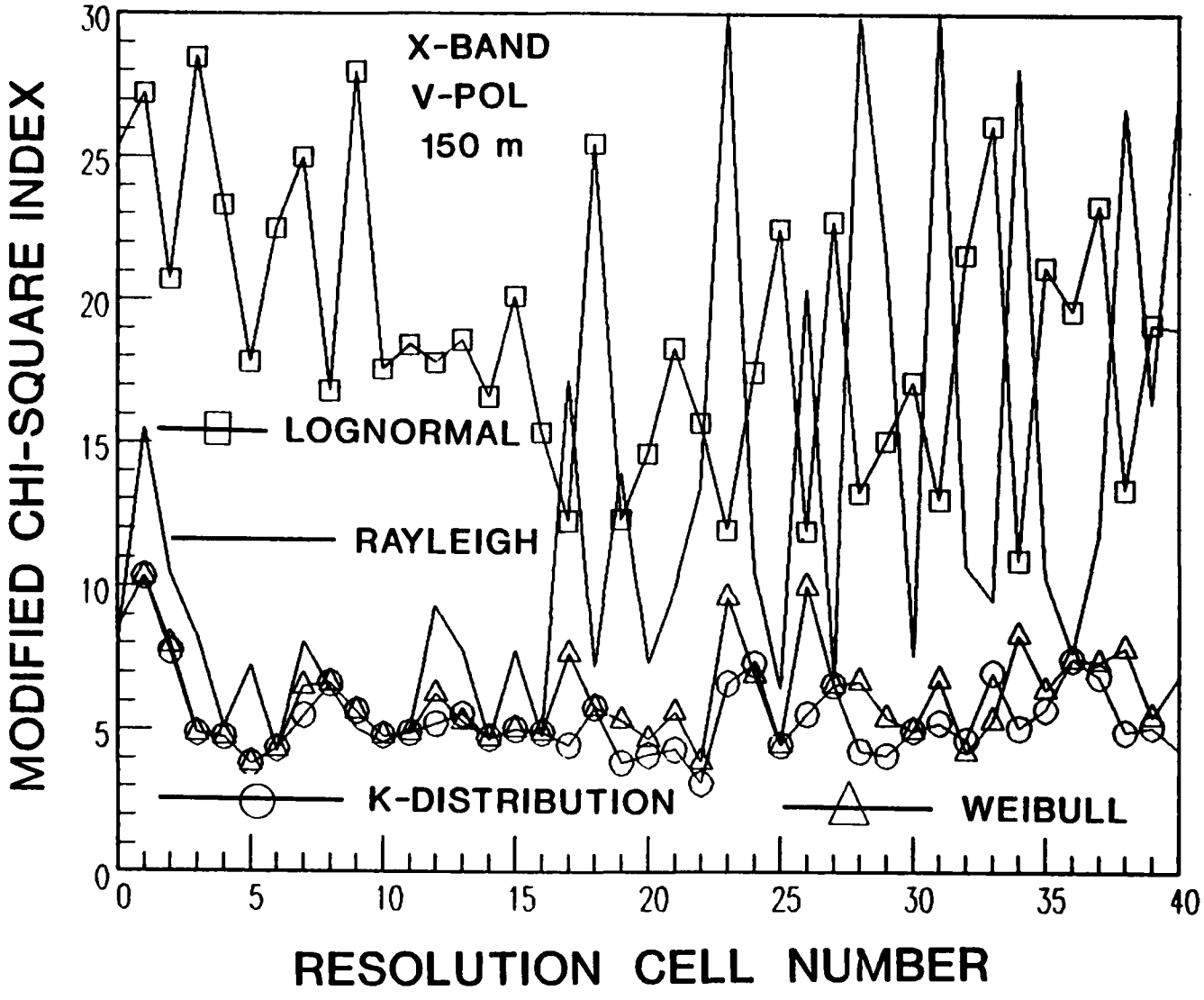

Figure 21 Comparison of the modified chi-square index of X-band, V-POL, 150 m resolution sea clutter computed for the Rayleigh, Weibull, lognormal and K-models for a group of resolution cells.

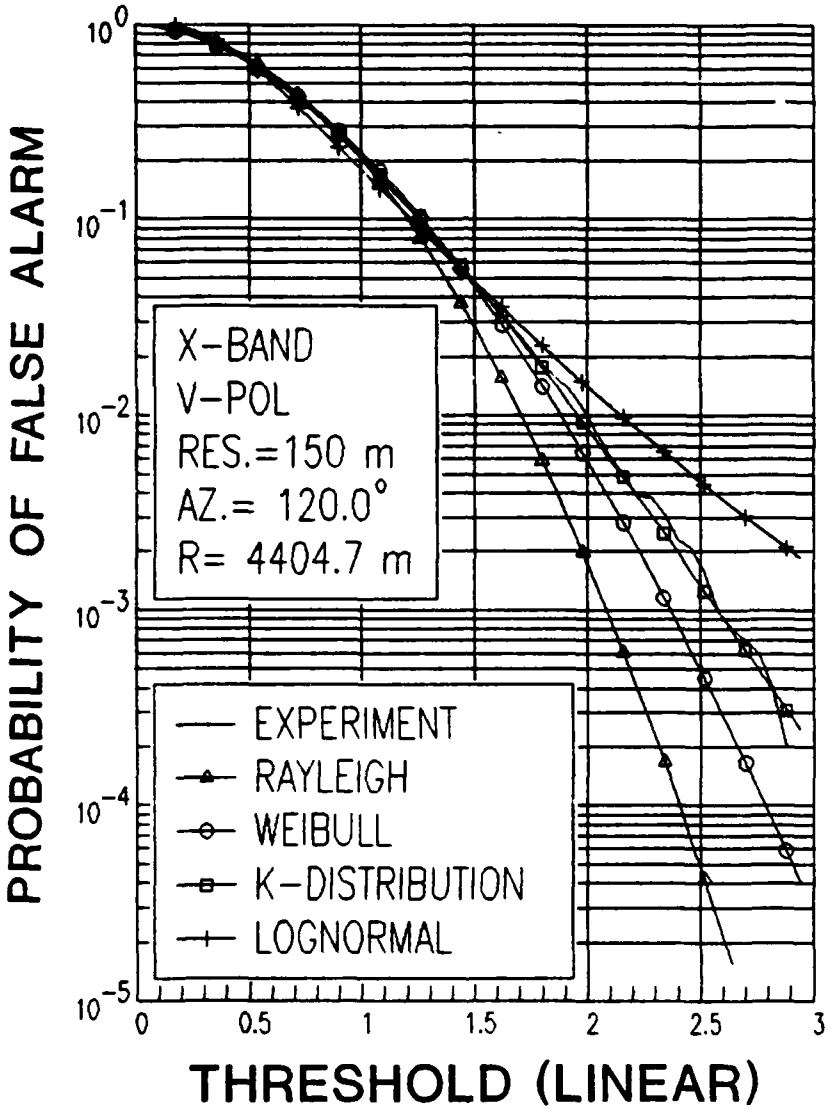

Figure 22 Comparison of the P_{fa} characteristics of a typical low resolution X–band, V–POL sea–clutter data set with those predicted by the Rayleigh, Weibull, lognormal and K models.

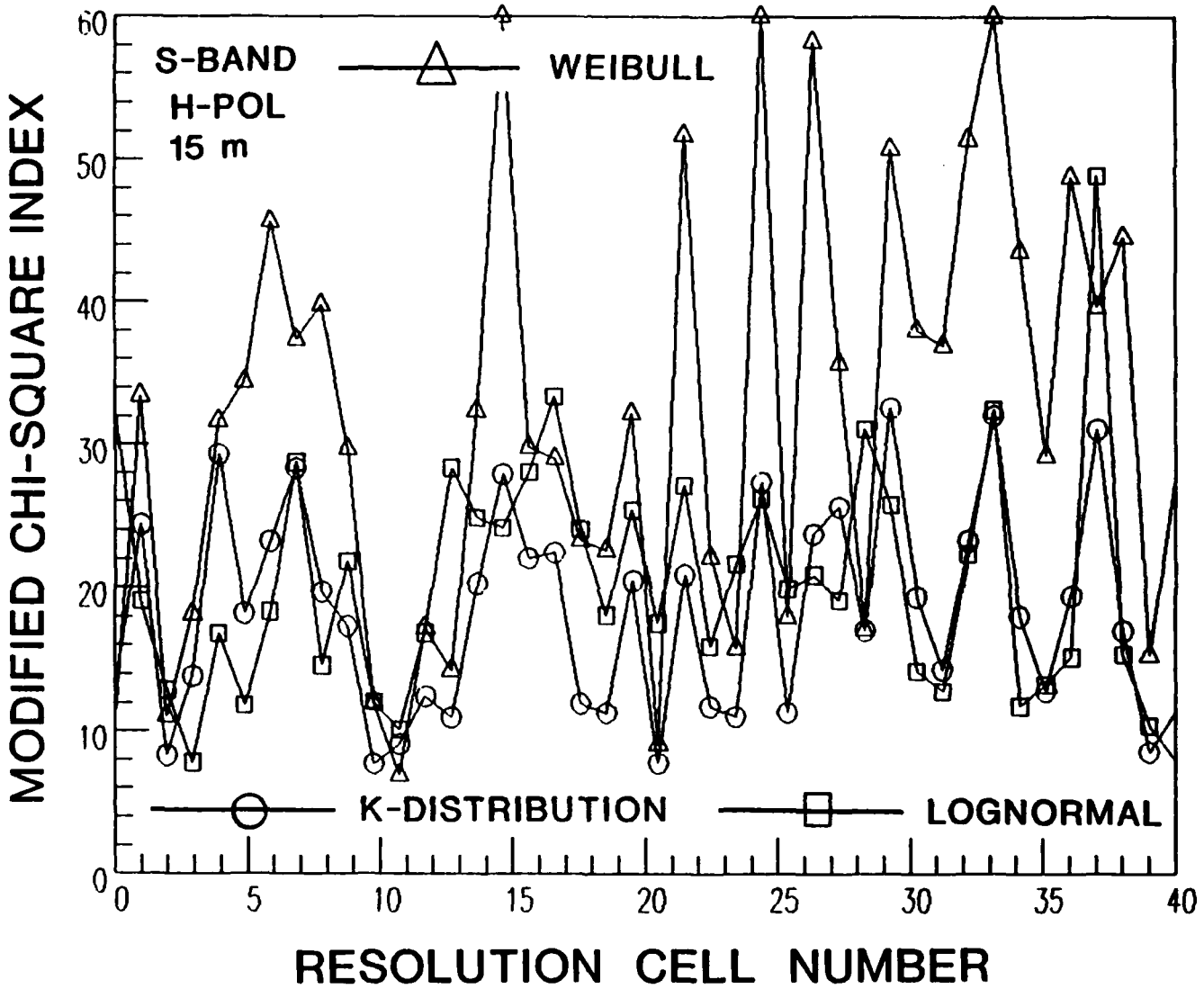

Figure 23 Comparison of the modified chi-square index of S-band, H-POL, 15 m waveform sea clutte computed for the Rayleigh, Weibull, lognormal and K models for a group of resolution cells.

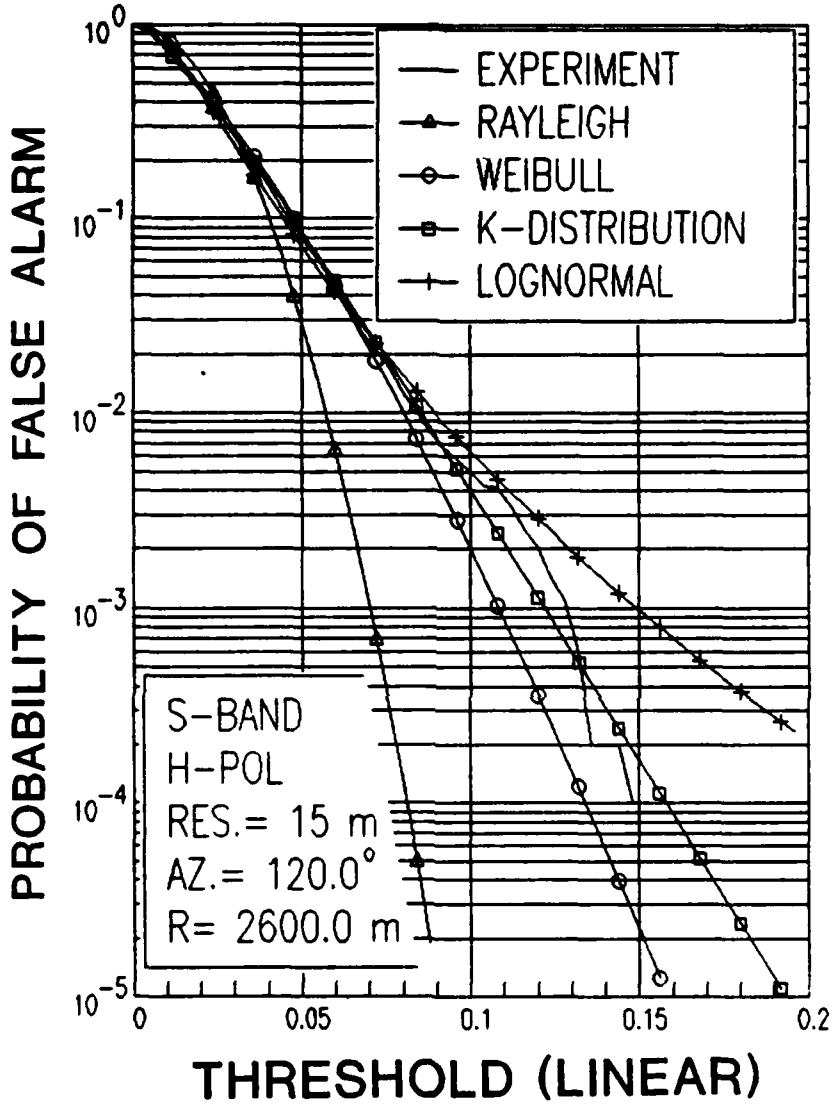

Figure 24 Comparison of the P_{fa} characteristics of a typical high resolution S–band, H–POL sea–clutter data set with those predicted by the Rayleigh, Weibull, lognormal and K models.

Table II. Summary of modified chi-square test on sea clutter

Band	POL	Res. (m)	Averaged modified χ^2 index				Sample size
			Rayleigh	Weibull	Lognormal	K	
X	V	150	18.11	10.57	22.96	9.46	80
	H	150	168.77	15.45	11.68	8.93	80
	V	15	150.2	9.99	15.18	7.51	160
	H	15	802.7	24.58	12.50	14.62	160
S	V	150	23.01	18.30	36.33	17.24	80
	H	150	361.80	20.52	19.14	13.00	80
	V	15	85.60	8.09	18.85	7.85	160
	H	15	423.01	31.19	23.38	18.99	160
L	V	150	15.43	12.02	23.42	11.85	80
	V	15	19.57	16.89	30.49	17.03	80

3.6 Sea Swell and Sea Spikes

One of the strange phenomena observed in sea clutter is that if sea spikes – random occurrences of abrupt increase of sea–clutter magnitude of time duration in the order of a second. Ward [18] identifies a component in the sea clutter having a spatially varying mean level as the result of the bunching of scatterers by sea–swell structures. Thus sea swell could also be responsible for the occurrence of sea spikes. The verification of this theory requires that the sea–clutter data be analyzed together with ground truth data (regarding the wave crest and heights, etc.) taken simultaneously. This type of ground truth data was not available for the North Truro experiment. Nevertheless, there were some high resolution data suitable for examining sea–spike phenomena.

3.6.1 Range–time–intensity plots.

A useful tool in analyzing sea clutter both spatially and temporally (in a time scale measured in seconds) is the range–time–intensity (RTI) plot. Here high–resolution (15 m) sea–clutter data taken from a number of resolution cells in a given direction for an extended period of time (20 seconds) were used to form a RTI plot.

The sample mean of the data was removed to suppress any possible ground clutter contribution from the antenna sidelobes. The squared magnitudes of the resulting time series were then summed over contiguous blocks of 100 samples. The result is a 100–point time series with each point representing the averaged clutter magnitude over a 200 msec time interval. This is done for data of 100 contiguous resolution cells. The resulting data set is then plotted in a 3–D format.

3.6.2 Vertically and horizontally polarized sea clutter at high resolution.

A typical RTI plot for an X–band, V–POL sea–clutter data set is shown in Figure 25. In this figure the x–dimension is range (100 points – 15 m per point), the y–dimension is time (100 points – 200 msec per point) and the z–dimension is the equivalent radar cross section (m^2).

Spectral analysis of this data set showed that the sea–clutter spectrum had a mean Doppler shift of 50 Hz, indicating that the water waves were moving towards the radar at a speed of about 0.82 m/sec. The RTI plot of this data set clearly showed the regular patterns associated with the wave crests and troughs. If we start from a certain resolution cell with a relatively high clutter magnitude a time zero, we can detect a gradual migration of the high clutter magnitude into progressively closer resolution cells.

From Figure 25, we measured approximately the distance over which a given high clutter magnitude migrated in 20 seconds to be 234 m. This corresponded to a phase velocity of 11.7 m/sec for the water wave. This phase velocity was not detected from spectral analysis because water particles or wave facets do not travel at the phase velocity. Indeed a velocity of 11.7 m/sec should give a Doppler shift of about 780 Hz at X–band. After accounting for aliasing, it did not match that obtained from spectral analysis (about +50 Hz). The Doppler shift measured from the sea–clutter spectrum represents the velocity of the water particles or wave facets, probably resulting from the effect of ocean currents.

Figure 26 shows the RTI plot for an X–band, H–POL data set. This experiment was performed about 6 minutes after the X–band, V–POL experiment (Figure 25). In this case we did not observed the regular wave–like pattern as we did in the case of the vertical polarization case.

The large clutter magnitudes of relatively short duration observed in isolated resolution cells were associated with sea spikes. In general, the H–POL sea spikes were significantly higher than the V–POL sea spikes. However, the magnitudes of the sea clutter during the time intervals between two sea spikes were much lower for horizontal polarization compared with those of the vertical polarization. In Section 3.6.3 we shall show the time waveforms of sea–clutter time series containing sea spikes and examine in greater details the spectrum of the sea spikes.

Figure 27 shows the RTI plot of another X–band, V–POL data set. In this case the look direction was perpendicular to that for the data set depicted in Figure 25. Since the look direction was near cross–swell, the regular wave–like patterns were not visible.

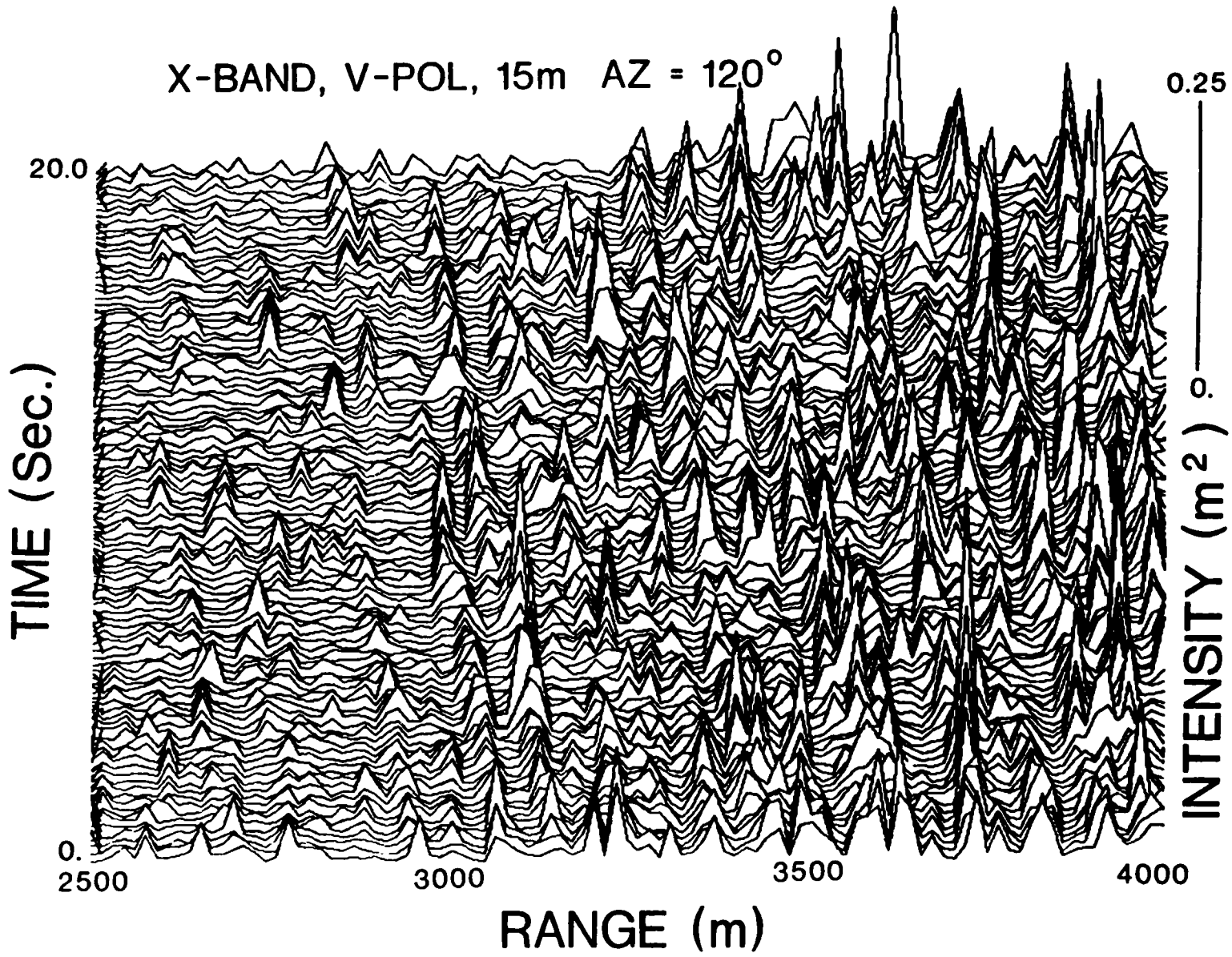

Figure 25 A typical RTI plot of X-band, V-POL, 15 m resolution sea-clutter data observed in the up-swell direction.

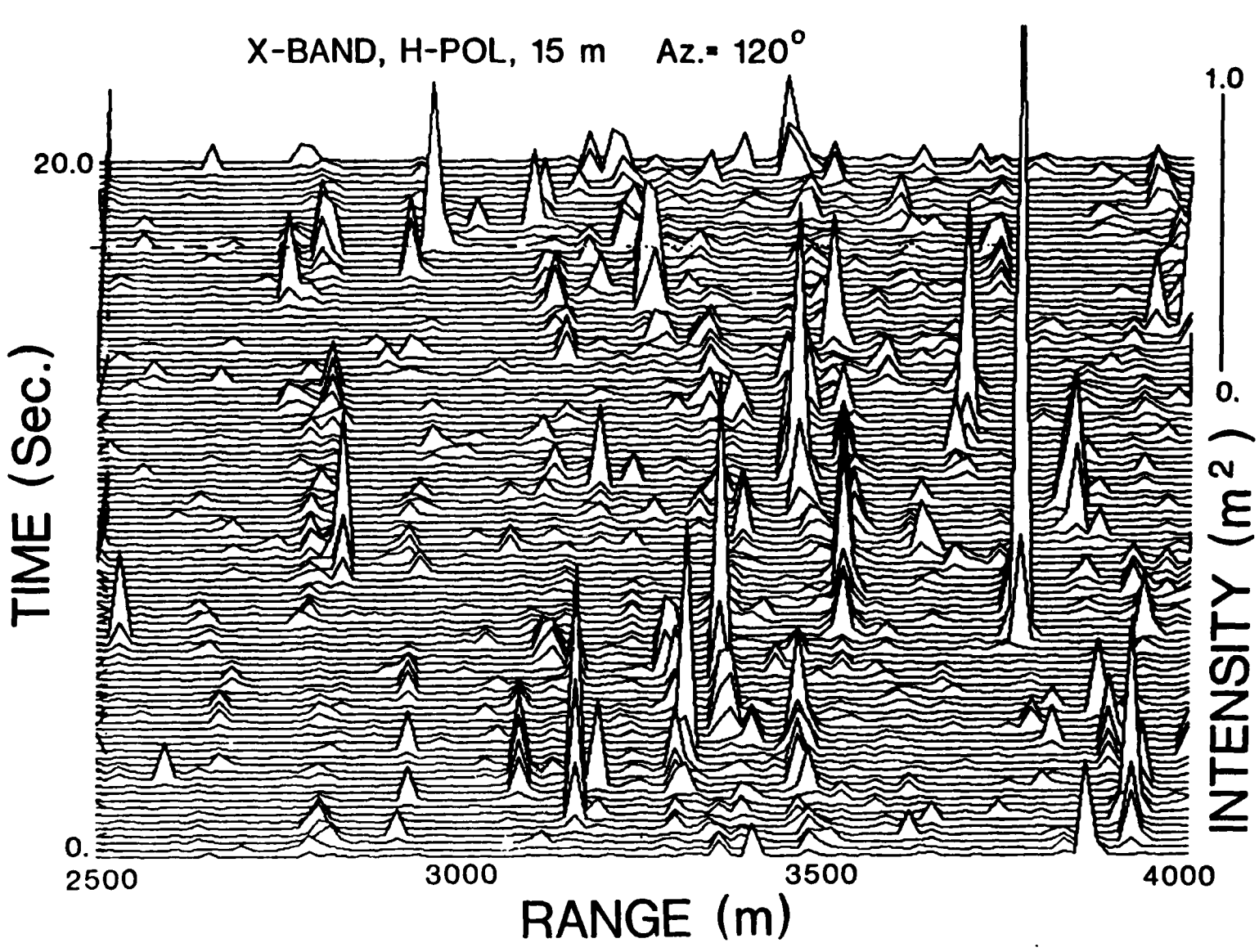

Figure 26 A typical RTI plot of X-band, H-POL, 15 m resolution sea-clutter data observed in the up-swell direction.

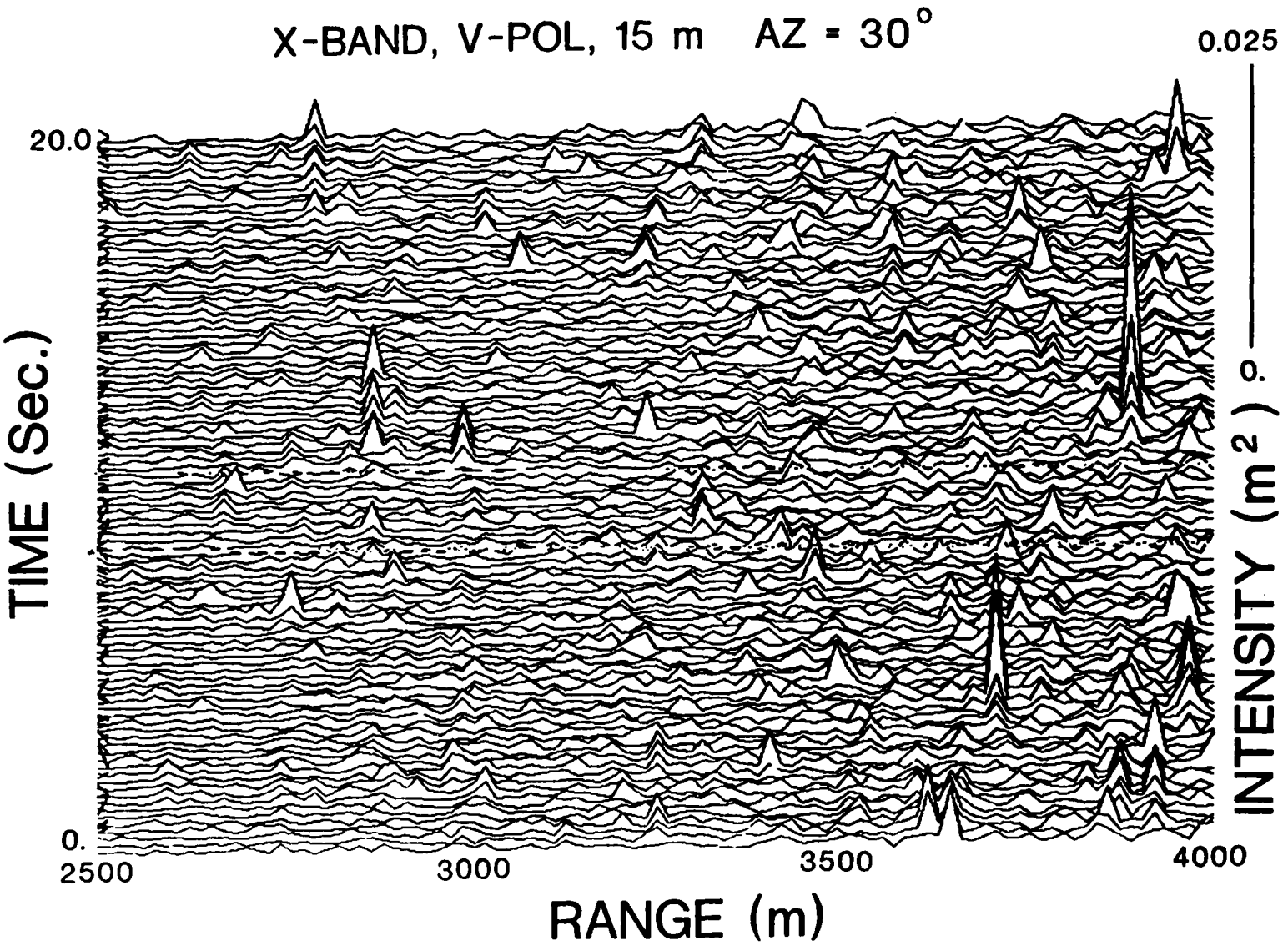

Figure 27 A typical RTI plot of X-band, V-POL, 15 m resdiution sea-clutter data observed in the cross-swell direction.

Similar results were obtained for the S–band cases. Figures 28 and 29 show the RTI plots for an S–band, V–POL and a H–POL sea–clutter data set, respectively. These experiments were performed about 10 minutes before the X–band experiments (Figures 25 – 27). Again the regular wave–like pattern was observed in the V–POL case, while a more spiky and random pattern was observed in the H–POL case. The phase velocity of the sea swell estimated from the S–band, V–POL RTI plot was in good agreement with those estimated from the corresponding X–band, V–POL RTI plots.

3.6.3 Temporal and Spectral Characteristics of Sea Spikes.

In this section we show several sea–clutter time series containing sea spikes. Figure 30 shows the in–phase waveform of an X–band, V–POL, 15 m resolution sea–clutter time series, together with the corresponding spectra computed for each two–second interval (called sectional spectra). The experiment parameters are shown in the figure. We observed several time intervals of duration in the order of two seconds in which the sea–clutter amplitude increased appreciably (e.g., pulses No. 3000 to 3800; 5000 to 6200; 7300 to 8000). The Doppler shifts and the spectral spread of the spectra computed for these segments of waveforms were substantially greater compared with those computed for segments with a lower clutter amplitude.

Figure 31 shows the in–phase waveform and the corresponding sectional spectra for an X–band, H–POL, 15 m resolution sea–clutter time series. In this case the sea–clutter amplitudes were fairly low during the 20–second time interval, except between pulses No.3100 to 3400, where a large spike appeared. The maximum instantaneous amplitude of the sea spike was almost 3 m, which corresponded to an RCS of about 9 m^2. We observed that the power and the Doppler shift of the spectrum for the waveform segment containing the sea spike was significantly greater than those of the other sectional spectra.

The results of Figures 30 and 31 suggested the following:

(a). The scatterers responsible for the occurrence of sea spikes have a greater velocity than those for ordinary sea clutter.

(b). The spectral power of H–POL sea clutter was dominated by that of the sea spikes.

Item (a) lends support to the theory associating the occurrence of sea spikes with sea swells. The sea waves will likely experience break–up at the crest of a sea swell. The large number of water particles thrown up by the breaking waves could explain both the greater magnitude and Doppler shifts (at X– and S–bands) of sea spikes.

Item (b) could explain the observed greater Doppler shift of the horizontal sea clutter compared with that in vertical polarization. If the contribution of H–POL spectral power comes mainly from those of sea spikes, then the average Doppler shifts of a H–POL sea–clutter spectrum will be greater.

Figures 32a and 32b show the averaged spectrum of the sea–clutter time series depicted in Figures 30 and 31, respectively. It is clear that, while the Doppler shifts of the sea spikes were similar for both vertical and horizontal polarization, the averaged Doppler shift of the spectrum in Figure 32b (H–POL) is greater than that of the spectrum in Figure 31a (V–POL).

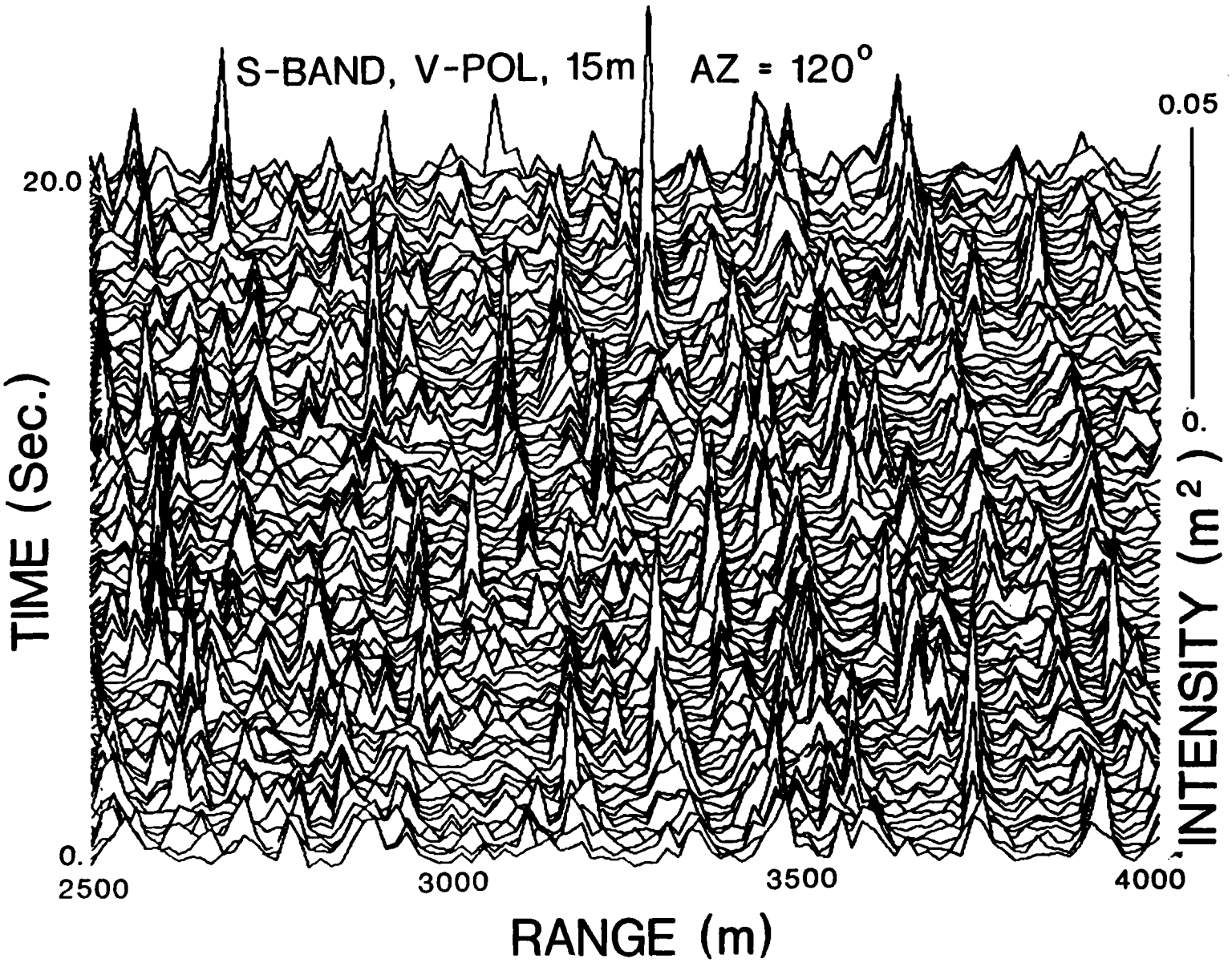

Figure 28 A typical RTI plot of S-band, V-POL, 15 m resolution sea-clutter data observed in the up-swell direction.

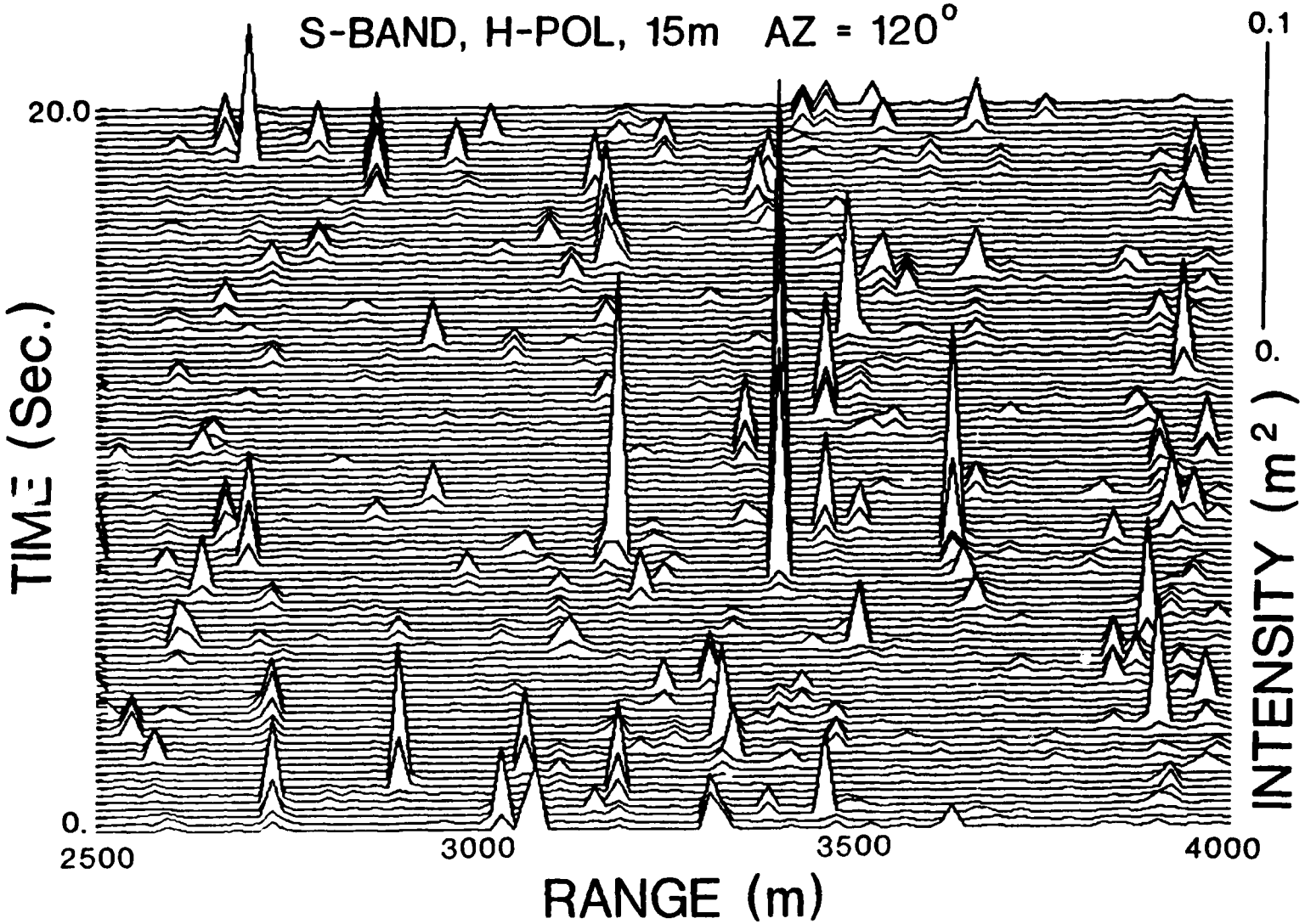

Figure 29 A typical RTI plot of S-band, H-POL, 15 m resoution sea-clutter data observed in the up-swell direction.

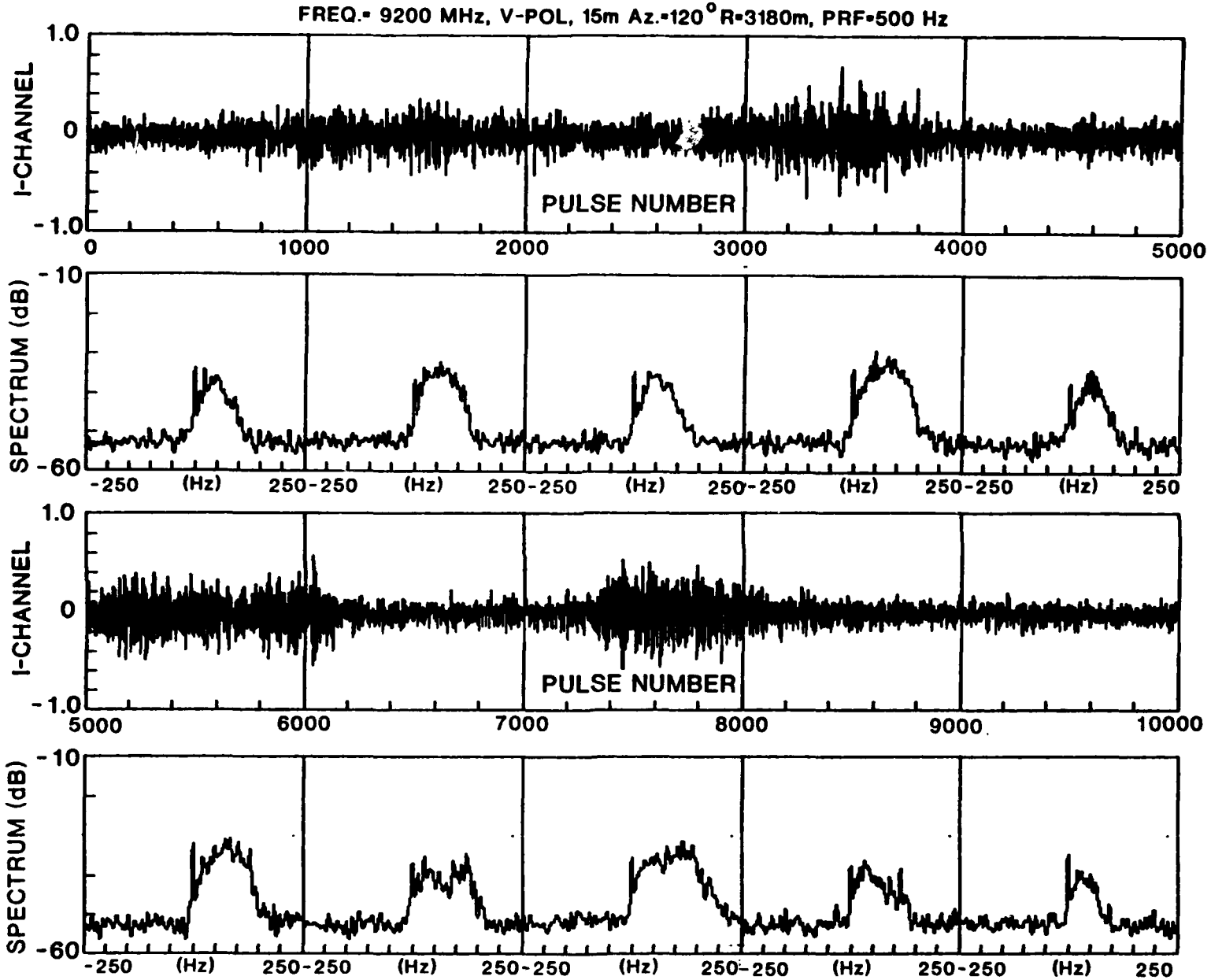

Figure 30 Time waveform and sectional spectra of an X-band, V-POL, 15 m resolution sea-clutter data set containing sea spikes.

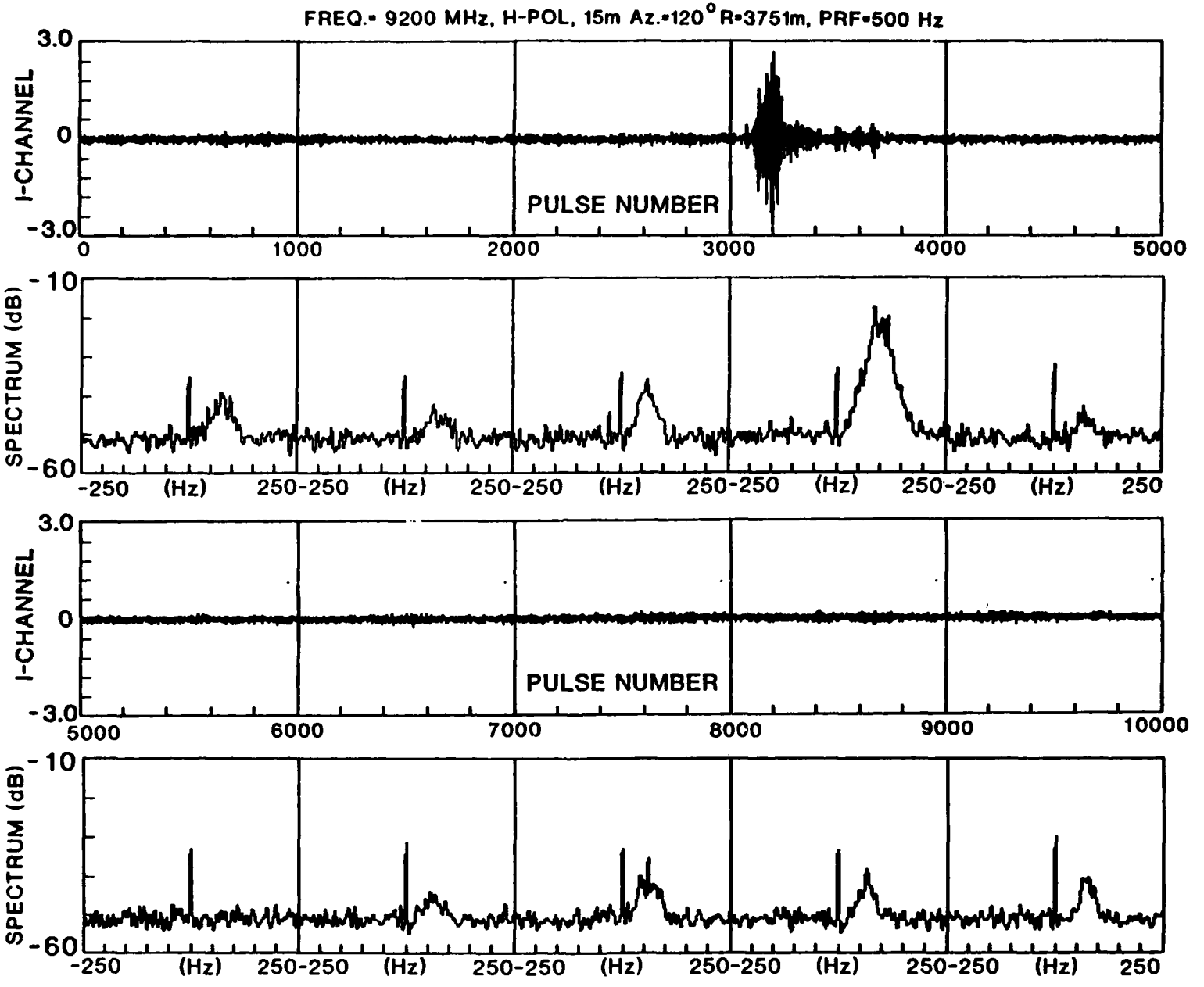

Figure 31 Time waveform and sectional spectra of an X-band, H-POL, 15 m resolution sea-clutter data set containing sea spikes.

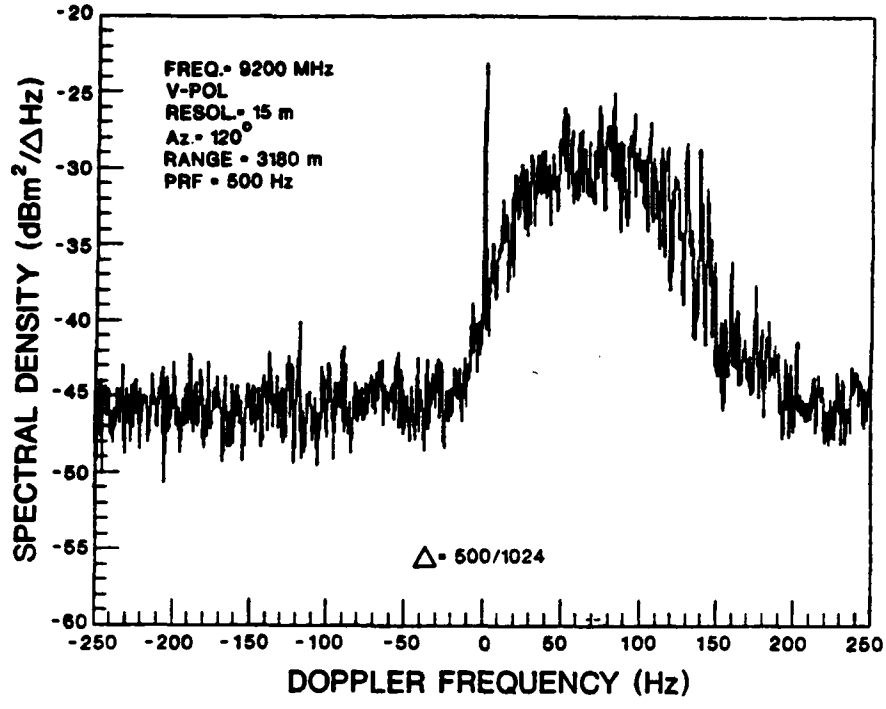

(a) V-POL

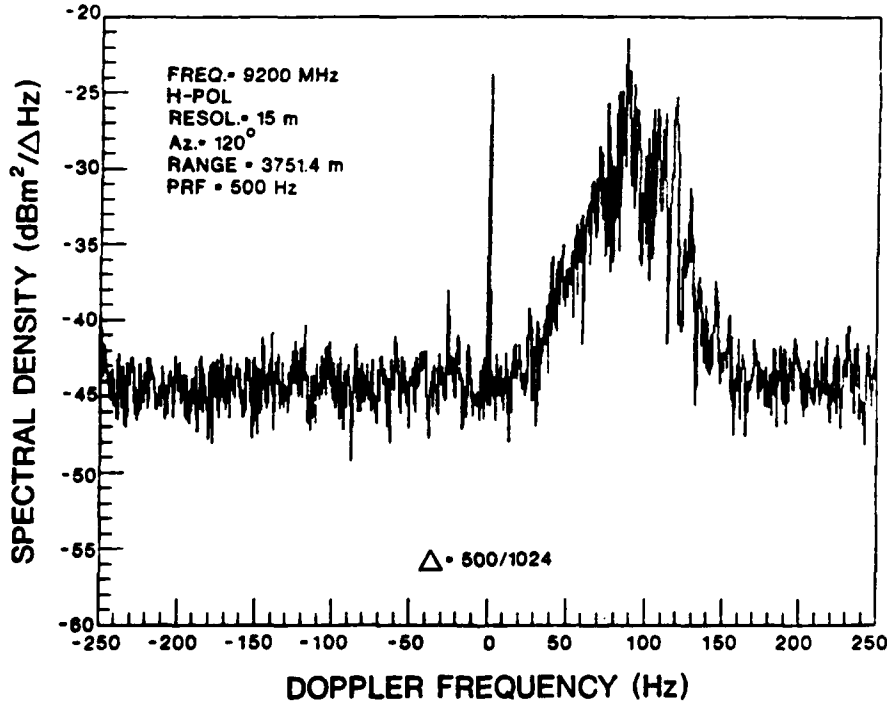

(b) H-POL

Figure 32 Averaged spectra of high-resolution X-band sea-clutter time series containing sea spikes.

4. SUMMARY AND CONCLUSIONS

An extensive analysis was performed on sea–clutter data collected in North Truro, Massachusetts. These data facilitated the examination of sea clutter over a wide range of frequencies and waveform resolutions under similar sea conditions. The results of the analysis supported the established theory that the three main mechanisms contributing to sea clutter are water droplets(sea spray), wave facets and Bragg resonance. The analysis provided insights into the conditions under which these mechanisms become dominant. For example, contribution to sea clutter of scattering by water sprays and droplets is important at high frequency bands (X and S). At L–band and lower the Bragg resonance effect began to dominate as evidenced by the concentration of spectral power around the characteristic Bragg Doppler shifts.

We compared the σ^o vs grazing angle results to the GIT and Sittrop sea–clutter models. Due to the limitations in the ground–truth data, we did not draw any conclusions with regard to the relative merits of these models. Instead, we presented the results together with some results calculated from the two models so that they can be qualitatively compared. More work is required to validate these predictive sea–clutter models in the low–angle region, particularly in conditions where ocean current is present.

Results of statistical analysis showed that sea–clutter amplitudes from a fixed resolution cell fit a K–distribution for all combinations of frequencies (among X–, S– and L–bands), polarization (V and H) and waveform resolutions (15m and 150m). The K–distribution fitting the data approached the limiting cases of a Rayleigh or a lognormal model depending on polarization, waveform resolution and frequency. For vertically polarized, low–resolution waveforms, sea–clutter statistics approached those of a Rayleigh model. For horizontal polarization and high resolution waveforms, sea–clutter statistics approached those of a lognormal distribution.

Spatial and temporal characteristics of sea spikes were examined through the use of RTI plots of high resolution sea clutter. The results supported the theory that sea spikes are associated with the wave crests in sea swells. This association was more evident from the V–POL RTI plots. For high resolution H–POL sea clutter, the clutter magnitudes were substantially lower than those observed with a V–POL radar; however, the magnitude of the sea spikes was generally higher than those in the V–POL case.

The theory explaining the differences between the V–POL and H–POL sea spikes is still incomplete. More data with better ground truth are needed to develop the theory and to improve sea–clutter models. One possible way to exploit this knowledge of sea–spike characteristics is to use a high–resolution radar with polarization diversity. Radar pulses are transmitted alternately with vertical and horizontal polarization. The vertical–polarization sea clutter can be used to obtain the sea–swell pattern which in turn can be used to predict the time of arrival of a wave crest. Target detection will be performed using the horizontally polarized returns. The detection threshold settings can be adaptively varied according to the estimated time of arrival of the wave crests.

The results presented in this report should be of use for maritime surveillance and shipboard radars where the grazing angle is generally low. However, it should be emphasized that these results were observed at relatively low sea states and should not be extrapolated to higher sea states without verification. Data at low grazing angles are scarce, particularly at lower frequencies.

The North Truro sea–clutter data which were coherent and collected in long–dwell mode provided reliable σ^o estimates for cases of very low clutter magnitudes (L–band, H–POL). This should provide more accurate information for low–angle sea–clutter modeling than available at present.

In conclusion, through the analysis of the North Truro data, we have obtained valuable information and additional insights into sea–clutter behaviour at low sea state and low grazing angle. However more data are needed, particularly at higher sea states, to develop and verify sea–clutter models.

5. REFERENCES

[1] N.W. Guinard and J.C. Daley, "An Experimental Study of a Sea Clutter Model", Proc. of IEEE, Vol.58, No.4, April 1970, pp. 543–550.

[2] G.V. Trunk, "Radar Properties of Non–Rayleigh Sea Clutter", IEEE Trans. on Aerospace and Elect. Sys. Vol.AES–8, No.2, March 1972, pp. 196–204.

[3] M.W. Long, "On the Polarization and the Wavelength Dependence of Sea Echo", IEEE Trans. on Antenna and Propagation," Vol.AP–13, No.5, September 1965, pp. 749–754.

[4] J.W. Wright, "A New Model for Sea Clutter", IEEE Trans. on Antenna and Propagation", Vol.AP–16, No.2, March 1968, pp. 217–223.

[5] J.B. Billingsley and J.F. Larrabee, "Multi–Frequency Measurement of Low Angle Radar Ground Clutter at 42 Sites", CMT–87, Lincoln Laboratory, to be published in December 1989.

[6] M.I. Skolnik, "Sea Echo", Radar Handbook, McGraw–Hill Book Company, New York, 1970, p. 26–4.

[7] J.B. Billingsley, "Phase One Master Directory File", MIT Lincoln Laboratory CMDT Project Memorandum No. 45 PM–CMT–0003, September 1985.

[8] A.V. Oppenheim and R.W. Schafer, "Digital Signal Processing", Prentice Hall, Inc., Englewood Cliffs, N.J., 1975.

[9] J.P. Burg, "Maximum Entropy Spectral Analysis", Ph.D. Thesis, Standford University, Standford, California, U.S.A., 1975.

[10] N. Andersen, "On the Calculation of Filter Coefficients for Maximum Entropy Spectral Analysis", Geophysics, Vol.39, 1974, pp. 69–72.

[11] V.W. Pidgeon, "Doppler Dependence of Radar Sea Return", Journal of Geophysical Research, Vol. 73, No.4, Feb. 1968, pp. 1333–1341.

[12] M.M. Horst, F.B. Dyer and M.T. Tuley, "Radar Sea Clutter Model", URSI Digest, 1978 International IEEE AP/S URSI Symposium, College Park, Maryland, U.S.A.

[13] H. Sittrop, "On the Sea–Clutter Dependency on Wind Speed", Proc. IEE Conference, Radar '77, London 1977.

[14] D.R. Thompson, "Calculation of Microwave Doppler Spectra from the Ocean Surface with a Time–dependent Composite Model", Radar Scattering from Modulated Wind Waves, (G.J. Komen and W.A. Oost Ed.), Klumer Academic Publisher, the Netherlands, pp.27–40, 1989.

[15] F.A. Fay, J. Clarke and R.S. Peters, "Weibull Distribution Applied to Sea Clutter", Proc. IEE Radar '77, London, October, 1977.

[16] I. Guttman, "Introductory Engineering Statistics", John Wiley and Sons, Inc., New York, New York, 1965.

[17] F. Jakeman and P.N. Pusey, "A Model for Non–Rayleigh Sea Echo", IEEE Trans. on Ant. and Prop. Vol. AP–24, No.6, November 1976, pp. 806–814.

[18] K.D. Ward and S. Watts, "Radar Clutter in Airborne Maritime Reconnaissance Systems", Military Microwaves, 1984, pp. 222–228.

[19] H.B. Mann and A. Wald, "On the Choice of the Number of Intervals in the Application of the Chi–square Test.", Ann. of Math. Stat., 13, 1942, pp. 306–317.

6. ACKNOWLEDGEMENT

The author thanks Group 45 of the MIT Lincoln Laboratory for providing the North Truro sea–clutter data under a Canada–U.S. Memorandum of Understanding. In particular, thanks are due Mr. J.B. Billingsley for useful discussions.

DOCUMENT CONTROL DATA

(Security classification of title, body of abstract and indexing annotation must be entered when the overall document is classified)

1. ORIGINATOR (the name and address of the organization preparing the document. Organizations for whom the document was prepared, e.g. Establishment sponsoring a contractor's report, or tasking agency, are entered in section 8.)

DEFENCE RESEARCH ESTABLISHMENT OTTAWA
3701 Carling Ave., Ottawa, Ontario K1A 0Z4, CANADA

2. SECURITY CLASSIFICATION (overall security classification of the document. including special warning terms if applicable)

UNCLASSIFIED

3. TITLE (the complete document title as indicated on the title page. Its classification should be indicated by the appropriate abbreviation (S,C,R or U) in parentheses after the title.)

ANALYSIS OF THE NORTH TRURO SEA CLUTTER DATA (U)

4. AUTHORS (Last name, first name, middle initial)

CHAN, HING C.

5. DATE OF PUBLICATION (month and year of publication of document)

SEPTEMBER 1990

6a. NO. OF PAGES (total containing information. Include Annexes, Appendices, etc.)

60

6b. NO. OF REFS (total cited in document)

19

7. DESCRIPTIVE NOTES (the category of the document, e.g. technical report, technical note or memorandum. If appropriate, enter the type of report, e.g. interim, progress, summary, annual or final. Give the inclusive dates when a specific reporting period is covered.)

DREO TECHNICAL REPORT

8. SPONSORING ACTIVITY (the name of the department project office or laboratory sponsoring the research and development. Include the address.)

DEFENCE RESEARCH ESTABLISHMENT OTTAWA, 3701 CARLING AVE., OTTAWA, ONT K1A 0Z4

9a. PROJECT OR GRANT NO. (if appropriate, the applicable research and development project or grant number under which the document was written. Please specify whether project or grant)

041LC

9b. CONTRACT NO. (if appropriate, the applicable number under which the document was written)

10a. ORIGINATOR'S DOCUMENT NUMBER (the official document number by which the document is identified by the originating activity. This number must be unique to this document.)

DREO REPORT 1051

10b. OTHER DOCUMENT NOS (Any other numbers which may be assigned this document either by the originator or by the sponsor)

11. DOCUMENT AVAILABILITY (any limitations on further dissemination of the document, other than those imposed by security classification)

- (X) Unlimited distribution
- ( ) Distribution limited to defence departments and defence contractors; further distribution only as approved
- ( ) Distribution limited to defence departments and Canadian defence contractors; further distribution only as approved
- ( ) Distribution limited to government departments and agencies; further distribution only as approved
- ( ) Distribution limited to defence departments; further distribution only as approved
- ( ) Other (please specify):

12. DOCUMENT ANNOUNCEMENT (any limitation to the bibliographic announcement of this document. This will normally correspond to the Document Availability (11). However, where further distribution (beyond the audience specified in 11) is possible, a wider announcement audience may be selected.)

UNLIMITED

UNCLASSIFIED

SECURITY CLASSIFICATION OF FORM

13. ABSTRACT (a brief and factual summary of the document. It may also appear elsewhere in the body of the document itself. It is highly desirable that the abstract of classified documents be unclassified. Each paragraph of the abstract shall begin with an indication of the security classification of the information in the paragraph (unless the document itself is unclassified) represented as (S), (C), (R), or (U). It is not necessary to include here abstracts in both offical languages unless the text is bilingual).

In this report we present the results of the analysis of sea-clutter data collected at North Truro, Massachusetts by the MIT Lincoln Laboratory. The data were obtained in conditions typical of sea state 2 at X-, S-, L-bands, UHF and VHF. We examined the data both spectrally and statistically. The results showed that sea clutter exhibited very different spectral characteristics at higher frequencies compared to those at lower frequencies. Experimental sea-clutter coefficients as a function of grazing angle at various frequency bands were obtained for up-swell and cross-swell conditions. Most sea-clutter models use the radar look direction relative to the wind direction as an input parameter (e.g., up-wind, cross-wind, etc). Hence a direct comparison of sea-clutter magnitude with those calculated from models under different wind conditions was not made. Instead, we showed these results together with those calculated from two sea-clutter models, assuming upwind and cross-wind conditions. The data were quite dissimilar in the low-grazing-angle regions to those predicted by the two models. Further research on sea clutter in the low-grazing-angle regions is needed to verify and explain the observed differences. We found the sea-clutter amplitude statistics fit the K-distribution best in the important low-probability-of-false-alarm region. The distribution approached that of a Rayleigh model for vertical polarization and low-resolution waveforms. However, there was a significant proportion of resolution cells with sea clutter having non-Rayleigh statistics even in relatively low-resolution waveforms and vertical polarization. For horizontal polarization and/or high resolution waveforms, the statistics approached those of a lognormal model. The statistical results provided further evidence that the K-distribution can serve as a limiting distribution for sea clutter. Spatial and temporal characteristics of sea spikes were examined through the use of range-time-intensity plots of high-resolution sea clutter. The results supported the theory that sea spikes are associated with the wave crests in sea swells. This association was more evident from high-resolution, V-POL sea-clutter data. The results of this report are pertinent to shipboard radar applications where the grazing angle is low. They also provide additional information for sea-clutter modeling in the low-angle region, particularly at the lower frequency bands.

14. KEYWORDS, DESCRIPTORS or IDENTIFIERS (technically meaningful terms or short phrases that characterize a document and could be helpful in cataloguing the document. They should be selected so that no security classification is required. Identifiers, such as equipment model designation, trade name, military project code name, geographic location may also be included. If possible keywords should be selected from a published thesaurus, e.g. Thesaurus of Engineering and Scientific Terms (TEST) and that thesaurus-identified. If it is not possible to select indexing terms which are Unclassified, the classification of each should be indicated as with the title.)

RADAR, SEA CLUTTER, SEA SWELL, SEA SPIKES

UNCLASSIFIED

SECURITY CLASSIFICATION OF FORM